

Rochester Institute of Technology

RIT Digital Institutional Repository

Theses

7-7-2022

Localized Surface Plasmon Resonance Enhancement from Complex Nanoscale Geometries

Jacob T. Waitkus
jtw2839@rit.edu

Follow this and additional works at: <https://repository.rit.edu/theses>

Recommended Citation

Waitkus, Jacob T., "Localized Surface Plasmon Resonance Enhancement from Complex Nanoscale Geometries" (2022). Thesis. Rochester Institute of Technology. Accessed from

This Thesis is brought to you for free and open access by the RIT Libraries. For more information, please contact repository@rit.edu.

RIT

Localized Surface Plasmon Resonance Enhancement from Complex Nanoscale Geometries

Jacob T. Waitkus

A Thesis Submitted in Partial Fulfillment of the Requirements for the
Degree of Master of Science in Material Science

School of Chemistry and Material Science

College of Science

Rochester Institute of Technology

Rochester, NY

07/07/2022

Committee Approval:

Approved: _____ Date:

Dr. Ke Du
Department of Mechanical Engineering
(Thesis Advisor)

Approved: _____ Date:

Dr. Nikhil Bhalla
Nikhil Bhalla Research Group
(Committee Member)

Approved: _____ Date:

Dr. Parsian Katal Mohseni
Department of Electrical and Microelectronic Engineering
(Committee Member)

Approved: _____ Date:

Dr. Patricia Taboada-Serrano
Department of Chemical Engineering
(Committee Member)

Approved: _____ Date:

Scott Williams
School of Chemistry and Material Science
(Director, MSE Degree Program)

Abstract

The unprecedented COVID-19 pandemic highlights the need for portable, sensitive, and accurate biosensors. Here, a novel biosensor that takes advantage of localized surface plasmonic resonance (LSPR) through unique nanoscale geometries was fabricated for sensitive detection of biomarkers. The formation of an adaptable system capable of combining with other sensing methods, such as CRISPR-Cas13a assays, allowed for the detection of specific targets to be realized. In this system, streptavidin-coated gold nanoparticles (GNPs) hybridize with single-stranded RNA (ssRNA) before binding to the surface of gold nanomushrooms (GNMs). Through LSPR enhancement, this binding event produces a red shift in the resonance wavelength peak due to changes in the refractive index surrounding the GNMs. Various concentrations, shapes, and diameters of nanoparticles were investigated to determine the greatest possible resonant shift. Through this work, the use of streptavidin-coated 40 nm AuNPs produced the greatest redshift at ~30 nm for concentrations greater than 500 pM. Packaged in a microfluidic cell, the device offers a novel strategy for the detection of biomarkers with minimal sample preparation and rapid, label-free detection. Expanding this process to include CRISPR-Cas13a proteins incorporates the advantage of collateral cleavage which further enhances the sensitivity of LSPR, a critical and far-reaching bottleneck specifically of concern in label-free biosensing.

List of Figures

Figure 1: Examples of (a) ESI and (b) MALDI ion sources [2].	2
Figure 2: Typical structure of PoC device [6].	5
Figure 3: Demonstration of a "hot spot" in a dimer system [9].	6
Figure 4: Diagram for CRISPR-Cas12a (Cpf1) complex attack on dsDNA target [18].	10
Figure 5: Differences between Class 1 and Class 2 CRISPR systems.	12
Figure 6: Sensing of target DNA by LSPR enhancement on gold nanomushrooms.	14
Figure 7: Extraction of biomarkers from biological samples for analysis [26].	17
Figure 8: Process described for recycling amplification for nucleic acid testing [37].	22
Figure 9: Changes in a surface condition on a transducer following hybridization for detection of a target [38].	23
Figure 10: Demonstration of the formation of gold nanoparticles through micellar exchange [48].	27
Figure 11: Demonstration for fluorescent detection by Cas12 and Cas13 cleavage [51].	32
Figure 12: 3-D schematic highlighting AuNM components [23].	34
Figure 13: SEM image of nanomushrooms [23].	34
Figure 14: Images of the a) AuNM substrate and b) constructed microfluidic cell.	36
Figure 15: Fluorescent spectra for three washes of FAM-DNA probes.	39
Figure 16: Diagram for the addition of AuNPs to the microfluidic cell.	42
Figure 17: Absorbance spectrum for observation of the redshift resulting from the addition of AuNPs to the AuNM.	43
Figure 18: Effect of AuNP diameter on the apparent redshift in resonant wavelength.	44
Figure 19: Redshift resulting from variations in AuNP coatings.	44
Figure 20: Observation of the effect concentration has on the LSPR resonant redshift.	45
Figure 21: SEM images taken of the AuNM substrate before (left) and after (right) the addition of AuNPs.	46
Figure 22: FDTD simulations were modeled according to the structures built (left). The resulting absorbance spectra for various numbers of AuNPs are shown (middle). This is	

compared to the experimental data put against a normalized unit (right) to demonstrate broadening.47

Figure 23: Electric field maps were produced for various XY (middle, right) and XZ (left) cross-sections of the AuNM with six AuNPs based on the simulations above. This was performed with the EM field polarized on the x-axis (left) and 45-degree angle (middle, right). These images were produced for 631 nm (left) and 623 nm (middle, right).49

Figure 24: The calculated wavelength delta from interparticle separation based on the plasmonic ruler equation (Eqn #1).50

Figure 25: Diagram of the off-chip cleavage activity in the presence of a target and non-target sequence for the release and application of AuNPs to the AuNM substrate.53

Figure 26: The resulting redshift from the CRISPR application for samples containing target RNA sequences.54

Table of Contents

Abstract	iii
List of Figures	iv
Table of Contents	vi
1.0 Problem Introduction	1
1.1 Introduction to Molecular Diagnostics	1
1.2 Overview of Point of Care (PoC) Devices	4
1.3 Discussion on Localized Surface Plasmon Resonance (LSPR)	6
1.4 Synopsis of CRISPR Technology.....	10
1.5 Combining CRISPR and LSPR Biosensing	13
2.0 Literature Review	16
2.1 Introduction to Nucleic Acid Detection (NAT)	16
2.2 Use of PoC Systems for NAT	20
2.3 Role of LSPR in PoC Devices	24
2.4 Employing CRISPR for Sensing Methodologies	29
3.0 Fabrication of Microfluidic Cell	34
3.1 Development of the AuNM substrate.....	34
3.2 Forming the PDMS device.....	35
4.0 Optimization of Surface Binding	38
4.1 Preparation of Reagents	38
4.2 Early Protocols	38
4.3 Direct Addition Protocol	42
5.0 Analysis of the Surface Condition	43
6.0 Verification of Binding via Simulations and Modelling	47
7.0 Demonstration of System for Detecting a Viral Target	52
7.1 Preparation of CRISPR Reagents	52
7.2 Adaptations for the CRISPR Application	52
7.3 Identification of the Viral Target.....	54
8.0 Conclusion & Future Work	55
9.0 Supplemental Information	57
9.1 Microfluidic Cell Fabrication	57
9.2 Absorbance Setup Construction	57

9.3	Thiol and Salt Aging Protocol	58
9.4	Direct Addition Protocol	58
9.5	Tables and Figures	59
10.0	REFERENCES.....	62

1.0 Problem Introduction

1.1 Introduction to Molecular Diagnostics

In the modern era of disease detection and treatment, therapeutics, and risk assessment, molecular diagnostics have proven to be a necessity [1]. This topic envelops a variety of techniques that combine medical testing and the science of molecular biology by observing biomarkers found in the genome or proteome of a virus or organism. A molecule or genetic sequence that is specific to the desired target and is easy to detect at a low cost comprises the essential components for optimal biomarkers [2]. Common biomarkers include proteins [2], nucleic acids such as DNA and RNA [2, 3], and antibodies [3], depending on if the proteome or genome is being analyzed. Current diagnostic methods exist for testing both the genome and the proteome, with tools such as mass spectrometers [2, 3], microarrays [4], and polymerase chain reactions (PCR) [1, 5].

Mass spectrometers are a common molecular diagnostic method, available in a variety of sizes and price ranges allowing a wide range of people access to the tool [2]. A mass spectrometer works by vaporizing a sample, then sorting the resulting ion vapor by mass-to-charge ratio and plotting against the intensity or frequency of the specific ratio value. To achieve this, the spectrometer is comprised of three main components, the ion source, mass analyzer, and detector. The ion source is responsible for converting the molecules from the sample into ions that are capable of being sorted and detected by the other main elements. There are several leading methods for ionization such as the electrospray ionization (ESI), which ionizes molecules from solution at a high voltage, or the matrix-assisted laser desorption/ionization method (MALDI) that creates ions through the use of an anchored solid matrix which promotes adsorption of the molecules and causes them to

crystallize along the surface. These methods are similar to each other as shown by the examples in **Figure 1**. Once these crystals come into contact with a laser, they undergo sublimation to form the ion vapor [2]. These techniques are both considered to be state-of-art ion sources for their ability to ionize small sample sizes on the order of micrograms, as well as macromolecules like proteins. The ability to ionize proteins allows for the sequencing of proteomes, something alternative ion sources fail to achieve.

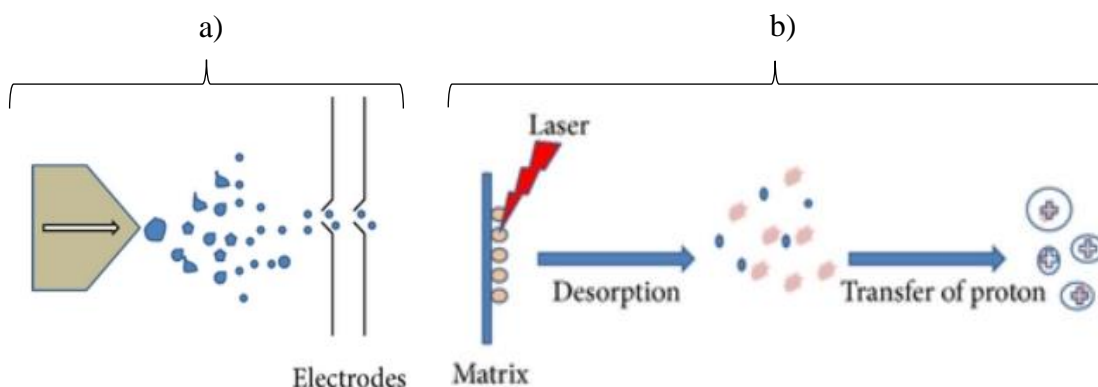


Figure 1: Examples of (a) ESI and (b) MALDI ion sources [2].

Used under [CC BY](#) / Cropped from original.

The mass analyzer component is responsible for the separation and sorting of ions resulting from the source by their mass-to-charge ratio. One of the common mass analyzers used in microsystems is a time-of-flight (TOF) unit [3]. In this system, ions are separated based on their kinetic energies and velocities, where ions of identical charge have the same kinetic energy. This system can be insensitive to macromolecules since they would require an acceleration of tens of keV for a reasonable signal to be obtained using a MALDI ion source [3]. Instead, Fourier Transform (FT) analyzers are often used to combat this issue. For this unit, charged particles are sent through a magnetic field, thereby inducing a circular trajectory on the ions due to the Lorentz force [3]. The frequency of the rotation can be measured and assigned to a specific mass value. The detector component used alongside

an FT system allows for the detection of multiple signals at once, which results in less noise and allows smaller peaks to be further analyzed. These units are extremely sensitive and can manage high throughput due to the multiplexed detection but come with the caveat of having a higher cost when compared to TOF systems.

Microarrays have seen a growth in popularity as a method for molecular diagnostics due to their usefulness in the mapping of genomes [4]. This method is a derivative of lab-on-chip devices, which are extensively used for multiplexed detection. Typically built on a solid substrate, such as glass or silicon, the arrays are capable of testing microquantities of biological materials. These arrays can be used to bind DNA or RNA probes with specific nucleic acid base sequences to the surface of the device [6]. The attached strands can be labeled with particular particles such as quantum dots or fluorophores to assist in detection. Following hybridization with the device, these label molecules will release an intensity signal proportional to the concentration of immobilized DNA or RNA strands in a given area [4]. This technique can be used to uncover gene expression or to identify single nucleotide polymorphisms (SNP) through the DNA or RNA hybridization process [4]. Since hybridization would only occur when the desired target is bound to the surface, no signal is reported when the target is absent from the sample. These devices can be combined with other diagnostic methods, such as mass spectrometers or fluorometers, to detect the fluorophores released from the hybridized reporter probes.

PCR is another primary method for molecular diagnostics [5, 6]. These reactions give the ability to replicate specific segments within a DNA strand using a DNA-polymerase enzyme. This enzyme is responsible for producing a complementary DNA (cDNA) sequence that matches the segment desired to be reproduced [5]. The complementary

sequence is known as a “primer” and is capable of producing billions of replicates of the desired target. Through amplification of the desired segment it becomes easier to identify and diagnose diseases found in the genome, as well as test for the presence of various other organisms or viruses in a sample. PCR is most valuable when used alongside other methods because of this ability to duplicate segments. The replication increases the concentration of the target within a sample, and therefore amplifies signal peaks to values greater than instrumental noise in many instances. This diagnostic method also makes observation of gene expression easier to achieve, where it may be difficult to know the role of certain sequences within a nucleic acid [5]. Due to the reproduction and wide-reaching capabilities, PCR methods have come to be known as the gold standard in molecular diagnostics.

1.2 Overview of Point of Care (PoC) Devices

In the face of our current pandemic with the SARS-Cov-2 virus variants affecting people on a global scale, the importance of rapid testing and diagnostics is apparent [7]. Multiple molecular diagnostic techniques have been used in the detection of viruses, along with the previous applications mentioned. But mass spectroscopy and microarrays are not often used in diagnosing various diseases. This is because many of the molecular diagnostic techniques are inefficient due to their bulky and expensive equipment, often requiring extensive prior knowledge of the process or trained laboratory workers to operate. A portion of these techniques require a standalone lab due to the size and cost of the instruments which affects the global availability of the techniques. This makes the process unfavorable and hard to scale to the level required for a pandemic-sized issue, highlighting the need for an effective PoC device.

PoC tools encompass a vast group of devices that are used for a variety of applications [6]. For instance, devices capable of detecting pathogens in water, blood samples, saliva, urine, or other fluids exist and are commonly utilized [5, 6, 8].

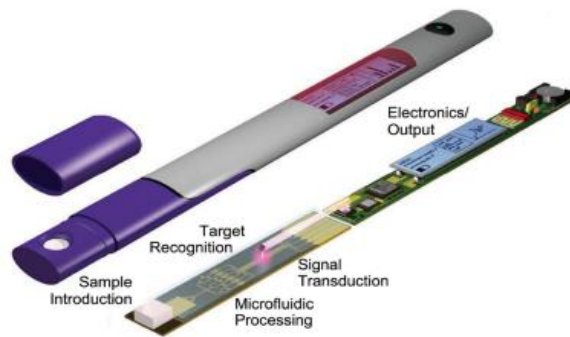


Figure 2: Typical structure of PoC device [6].

These devices can be constructed to test for both proteins and nucleic acids, as well as

Reprinted with permission from Gubala et al., 2012. Copyright 2012 American Chemical Society.

many other molecules and pathogens, much like molecular diagnostic techniques. PoC devices are even capable of containing select molecular diagnostic methods such as PCR [5, 6]. The ability to duplicate DNA sequences makes these devices attractive for their high sensitivity and selectivity, but at the cost of longer response times and higher costs associated with the PCR amplification [6]. PoC devices are defined by their ease of use and compactness which is illustrated in **Figure 2**. Their ability to be used practically anywhere, requiring only microsamples to provide accurate results is another crucial advantage of PoC systems. This is referred to as “near patient” testing. Since the goal of a PoC device is to be able to be used in vitro with minimal knowledge of the process, this is a big advantage over bulky or complex molecular diagnostic techniques like mass spectroscopy [6]. In order to be applicable for at-home testing, PoC tests need to be elementary in operation, meaning they are processes that can be self-administered by patients or consumers. As a result of the current pandemic limiting travel and gatherings, among other things, a test that can be administered at home or without the presence of medical professionals helps to prevent any further spreading of the disease and lower the

response time in isolating or treating the virus [6]. Limiting contact with infected individuals is paramount to slowing the pandemic and with the use of PoC devices it becomes a more achievable goal.

1.3 Discussion on Localized Surface Plasmon Resonance (LSPR)

An emerging technology for in-depth nanoscale detection is LSPR. This method provides a replacement for processes previously utilizing PCR as an amplification technique. LSPR allows for label-free detection of molecules bound to the surface of nanoparticles or nanostructures through shifts in optical resonance due to changes in the surrounding refractive index (RI) [8]. This technique provides a real-time detection method that can be used for any target that can be immobilized on the surface of the substrate. LSPR is capable of this advantageous detection by enhancing incident light waves that travel through “hot spots” between resonating nanoparticles of specific materials, as shown below in **Figure 3**. The resonating particles used for the enhancement of light must have

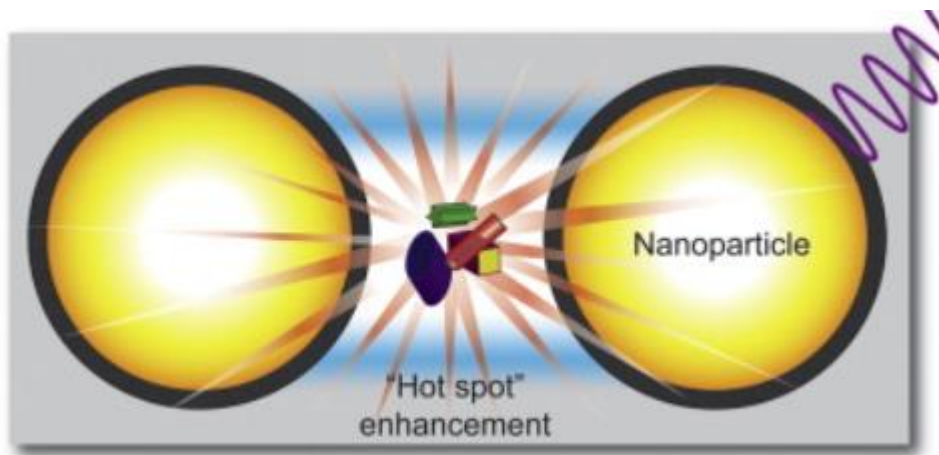


Figure 3: Demonstration of a "hot spot" in a dimer system [9].

Reprinted from Analytica Chimica Acta, Volume 706, Eleonora Petryayeva, Ulrich J. Krull, Localized surface plasmon resonance: Nanostructures, bioassays and biosensing - A review, Pages 8-24, Copyright 2011, with permission from Elsevier.

controlled dimensions since minor differences can affect the sensitivity and resulting resonant peaks observed [8]. Coinage metals, often gold, silver, or copper, are typically used in the fabrication of LSPR substrates due to their light adsorption strongly occurring in the visible region of the spectrum, among other advantages [10]. Nanoparticles made from coinage metals also exhibit high mobility of valence electrons that can be easily observed with common detection instruments. Their free electrons undergo an oscillatory effect due to the positively charged nuclei that resist the relaxation of these electrons. Due to the constant movement of electrons, an electric field forms around the nanoparticles when electrons are excited by the presence of incident light [10]. For this event to occur, the frequency of these incident photons must match the frequency of the valence electron oscillation which in turn, produces the surrounding electric field [10]. The use of gold is also popular as it is fairly chemically inert, meaning a gold substrate would be less likely to react with the surrounding solutions and media. The variety of chemicals that gold can resist opens up the device to more opportunities and expands the applicability of the system. Other than the materials used in the substrate, the particular optical resonance peak at certain wavelengths depend on their surface conditions as well. This includes the binding of citrate molecules, which aid in preventing aggregation of aqueous nanoparticles, or streptavidin molecules among various other desirable surface chemistry changes. The streptavidin molecule forms an ultra-strong covalent bond with biotin molecules which can be used as end groups on DNA or RNA strands.

LSPR is a variation on surface plasmon resonance (SPR), operating on similar principles. The greatest difference between the two methods is the location of where the plasmons are excited. SPR utilizes propagating surface plasmons which are excited on thin

metallic films, while LSPR will excite localized surface plasmons on nanoparticles, which can come in a variety of forms [11]. LSPR shows enhanced sensitivity to localized electron fields surrounding the particles compared to the resonance on metallic substrates from SPR methods. The increased sensitivity of LSPR techniques is further aided by dark-field imaging [12]. Dark-field images are created by scanning for the intensity of scattered light resulting from incident photons across the gaps between nanoparticles or at specified biosensing locations [12]. LSPR can be sensitive enough to detect even single-molecule binding events on the surface of a nanoparticle by observing the shift in the RI around the particle in the presence of scattered light [12].

LSPR can undergo both radiative and non-radiative decay following excitation by incident light. Radiative decay is a result of the scattering of resonant photons, while non-radiative decay is directly caused by Landau damping [10]. Landau damping is a unique effect that occurs when the resonant surface plasmons decay into electron-hole pairs [13]. The formation of these electron-hole pairs is at the highest rate in the previously mentioned “hot spots” located between adjacent nanoparticles [14]. Through the coupling of nanoparticles to form dimers, these “hot spots” or areas of enhancement are created. Light passing through these areas amplifies the resulting wavelength signal to approach intensities millions of units higher than the original signal [14]. With the further addition of nanoparticles to form larger multimers, the oscillation of the particles is important in increasing the efficiency of “hot spots” in creating electron-hole pairs. The enhancement within dimers is best seen when the particles are oscillating in phase, which means in the same direction at the same speed, as opposed to against each other. At higher levels such as trimers, multimers, and up to vast arrays, the number of possible resonant configurations

increases which can change the locations and intensities of the various “hot spots.” With more particles, such as in an array, the enhancement effects resulting from “hot spots” can increase even further with specific particle resonance. These electron-hole pairs have many applications other than use in LSPR making these systems valuable. One such application for these pairs is inorganic semiconductors, where the electron-hole pair has high mobility and can distribute a charge through a substrate’s lattice structure. Both radiative and non-radiative decay processes have exciting applications as well, particularly in the excitation of certain adsorbates and charge transfer from nanoparticles to the adsorbates. The excitation of other molecules by resonant photons is limited only to molecules that possess an energy gap between the highest occupied molecular orbital (HOMO) and the lowest unoccupied molecular orbital (LUMO) that is identical to the energy of the photons used in excitation [10]. This charge transfer system is used as the driving mechanism for many photoreactions. The electrons from the electron-hole pairs will move into the LUMO band of the bound molecules creating negatively charged particles which help to stabilize and drive certain dissociation reactions [10]. Electron-hole pairs have also been shown to produce photothermal effects when the hot electrons relax [14]. Therefore, these LSPR systems can act not only as a detection system for biomolecules, but as a catalyst for reactions by producing electron-hole pairs that accelerate the kinetics of a reaction in presence of incident light waves. Since these mechanisms can be the driving steps in several other reactions, the application of LSPR expands into fields that might not seem related to biosensing.

1.4 Synopsis of CRISPR Technology

Alternate methods exist for viral detection of DNA other than PCR amplification, in the form of clustered regularly interspaced short palindromic repeats (CRISPR). Through the study of bacteria and archaea, CRISPR and CRISPR associated systems (Cas) were first observed [15]. The CRISPR-Cas complex has become one of the fastest growing fields with vast applications

across several aspects of microbiology. The versatility and specificity of these systems allow for the detection of both DNA and RNA molecules, as well as testing for SNP and single nucleotide variations (SNV) on a smaller scale [16, 17]. In the presence of a particular DNA or RNA molecule, CRISPR tools can be specially designed for detecting a specified sequence within the strand. This is often achieved through a single guide RNA (sgRNA) in conjunction with a Cas protein to either break a double-stranded DNA molecule (dsDNA) in order to bind to the target strand, or to bind with a ssRNA at a particular location [17]. The sgRNA portion is formed by combining CRISPR RNA (crRNA) and transactivating RNA (tracrRNA) [19]. Therefore, the sgRNA is highly customizable as the nucleotides contained within the two RNA materials can be adjusted for various target sequences in a wide array of applications [17]. The other component in nucleic acid detection is the Cas protein. Nearly all types of CRISPR-Cas systems contain

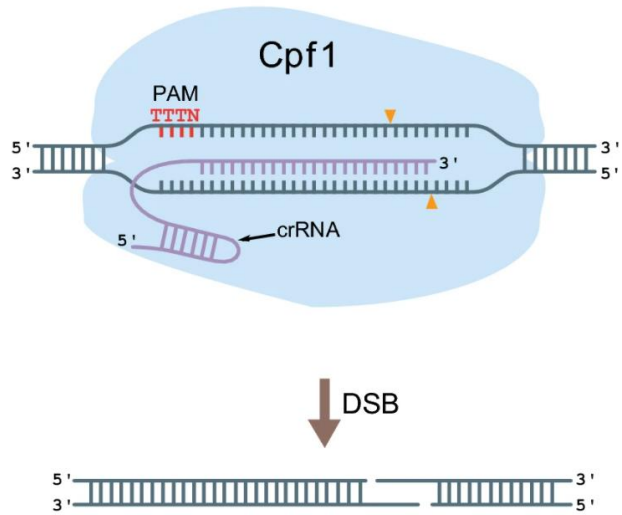


Figure 4: Diagram for CRISPR-Cas12a (Cpf1) complex attack on dsDNA target [18].

Used under [CC BY](#) / Cropped from original.

Cas1 and Cas2 proteins. These two are responsible for the adaptation of the infecting or target DNA and are spacers in the CRISPR locus at the leading end of the complex [20]. In order to aid the sgRNA in recognition of the particular target sequence, a protospacer-adjacent motif (PAM), or a PAMmer in the case of ssRNA, is used [20]. The PAM exists adjacent to the target region on the complementary strand of the target molecule which promotes the Cas protein's hybridization with the target. For positive detection of binding, labeling the target strand with fluorescence particles at one end is common practice. These fluorophores are released once hybridization occurs, producing a measurable signal. This can also be combined with quenching end labels which allow for easier detection of released fluorophores by covering unbound probes. CRISPR-Cas systems can also be used in the detection of point mutations or SNV in DNA or RNA strands when looking for a particular nucleotide base change [21]. The Cas proteins lack sensitivity to find randomized variations since the target sequence would fail to match the sgRNA of the system. In looking for diseases caused by SNV, such as sickle cell anemia, CRISPR systems can identify and potentially replace the abnormality by looking for the complementary strand to the point variation which avoids the reduced sensitivity [21]. This is achieved through a nicking process of the endonuclease, where once the system identifies the target sequence with the abnormality, the protein breaks the side of the dsDNA containing the wrong base pair to mark it for replacement by natural cell processes for DNA repair [21]. This process shows a promising future for further development that could lead to the cure of diseases and ailments once thought to be permanent afflictions.

Due to the high number of distinct CRISPR-Cas systems discovered, they were separated into two overarching classes each containing three subdivisions referred to as types. The classes are defined by the effector complex within the system where class 1 arrangements contain multiple crRNA effector complexes, typically ranging from four to seven Cas proteins [22]. Type 1 and 3 subsystems are similar and are both contained within class 1 but utilize different assemblies to achieve their function. Type 1 systems organize the effector complexes into a CRISPR-associated complex for antiviral defense (Cascade) complex, which is a combination of multiple Cas proteins. Meanwhile, type 3 subsystems apply Csm or Cmr proteins to achieve nucleic acid cleavage [15, 19]. Class 2 systems use single-effector proteins which differs from class 1 complexes where multiple Cas molecules are used as illustrated above in **Figure 5** in the effector region. Type 2 is the most well-defined subdivision of class 2, containing the single complex Cas9 protein. This protein is comprised of two nuclease domains, HNH and RuvC, which are responsible for target displacement and sequence cleavage [15, 22]. Type 5 systems are a more specific classification when compared to type 2 since this division of proteins is defined by a single

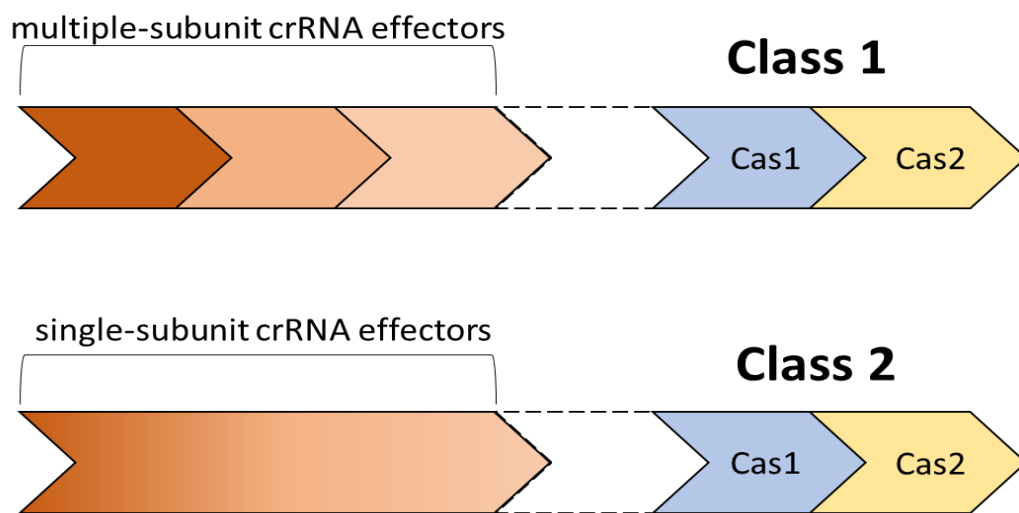


Figure 5: Differences between Class 1 and Class 2 CRISPR systems.

RuvC endonuclease domain, such as Cas12 proteins [19]. The majority of CRISPR-Cas systems are proficient only in the cleavage of DNA with the exception to type 2, 3a, and 3b which have the capability to target RNA strands, and class 2 type 6 systems that contain two HEPN domains (Higher Eukaryotes and Prokaryotes Nucleotide-binding) which contain Rnase activity for RNA strand targeting and cleavage [22]. These two domains are contained within a single effector protein known as c2c2 or Cas13a and are capable of targeting ssRNA which is identified by complementary crRNA strands [15]. Cas13a also has the unique advantage of non-specific cleavage following the binding and cleavage of the target strand [17, 21]. This property allows CRISPR-Cas13a systems to have potentially higher signal amplification when identifying target sequences or mutations within them. By adding RNA reporter probes into the solution with the test sample, a rapid response detection method is possible. If the reporter probes are cleaved through the collateral cleavage of Cas13a, that would imply that the target strand was present in the solution since the non-specific cleavage only follows the degradation of the target sequence [17]. This idea can also be used for the detection of point mutations where if the target strand contains a variation in the nucleotide sequence that is different than the gRNA, there will not be target cleavage and therefore, no output signal from the reporter probes since they will not be degraded by the CRISPR-Cas complex [21].

1.5 Combining CRISPR and LSPR Biosensing

CRISPR and LSPR technologies offer encouraging results in advancing the capabilities of PoC devices. Currently, a tool combining the advantages of both methods has yet to be developed. Light enhancement that results from an LSPR plasmonic device offers a label-free detection method for analytes that can bound to the surface.

Here, preceding the target nanoparticle being attached to the nanostructures, a CRISPR system is used to cleave ssRNA in the presence of SARS-CoV-2 in solution which would free AuNPs for later binding to the surface of the plasmonic chip. The Cas protein would cleave the nucleic acid if the solution contained the specified target sequence described above. By comparing the peak of the absorbance spectrum before the CRISPR system was introduced to a shift in the peak value can be observed indicating the AuNP was present on the surface and the target was in solution. This combination of biosensing methods offers high sensitivity and specificity in detection of nucleic acid sequences. As well as offering fast turnaround times in PoC devices, this pairing of LSPR and CRISPR systems provides consistent and repeatable results. The combination of label-free detection methods, the ability to evaluate dilute samples, and the small size requirement for LSPR substrates, lead to a portable PoC device capable of use as a ‘near-patient’ device.

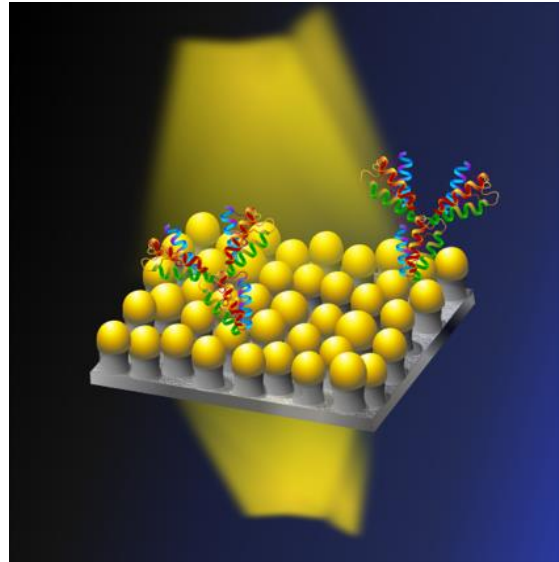


Figure 6: Sensing of target DNA by LSPR enhancement on gold nanomushrooms.

Reprinted with permission from Dr. Nikhil Bhalla and Professor Amy Shen (Micro/Bio/Nanofluidics Unit OIST).

Through the combination of both LSPR and CRISPR techniques, a portable PoC device capable of high sensitivity detection of ultra-dilute samples in a cost-effective manner became achievable. For this process, viral RNA molecules were cleaved off-chip to release AuNPs to the surface of the plasmonic chip. These are bound to the AuNM substrate via a direct addition protocol which offers a linker-free method for binding. The plasmonic chips

contained approximately 10^6 nanomushroom structures on a 1 cm^2 glass chip. These nanomushrooms are crafted from silicon dioxide pillars, capped by gold nanoparticles which are capable of detecting zettamolar quantities of the target analyte by taking advantage of the signal enhancement resulting from LSPR between caps [23]. The three-dimensional structures provide greater surface area allowing for higher bonding of the analyte system. The plasmonic chip was adhered to a glass substrate and covered by specific PDMS mold before the addition of the nanoparticles occurred. Through the addition of AuNPs, it was observed that the peak resonant wavelength underwent a gigantic redshift of 30 nm. Combined with the label-free advantages of LSPR and the size of the substrate the system is low cost and highly portable, while still maintaining high sensitivity and the ability for real-time detection. This is further exemplified by the CRISPR combination which used collateral cleavage to increase the sensitivity of the system, without requiring amplification of any components.

2.0 Literature Review

The accompanying literature review section outlines the basic techniques used in combination that led to the detection of viral DNA on gold nanomushrooms through the first device to combine CRISPR cleavage techniques and LSPR signal enhancement. This includes the development of PoC systems, and the many accompanying techniques utilized for detection. As well as the incorporation of LSPR into PoC devices in conjunction with CRISPR systems for biosensing applications. The following literary review section opens with a review of nucleic acid detection techniques.

2.1 Introduction to Nucleic Acid Detection (NAT)

The expansion of studies in nanoscience and microbiology has led to the growing use of biomarkers in testing. As previously stated, biomarkers can range from antibodies in blood to exosomes containing proteins and nucleic acids like DNA and RNA. The use of biomarkers provides healthcare professionals with the advantage of early disease detection before symptoms begin to show [8, 24]. This can include many neurological diseases, as well as internal issues with nearly all bodily systems. Biomarkers are also used for studying gene expression where hereditary diseases and ailments are often screened for. The different uses of biomarkers lead to most biomarkers falling into two major categories, biomarkers of exposure and biomarkers of disease [24]. Exposure markers are used to analyze the effects of environmental conditions and risk factors on an organism [24]. By incorporating samples of blood, hair, or other biomarkers, the detection of toxins and their concentrations can be used to determine the risk and health concerns posed by the foreign substances. Biomarkers of disease are crucial in detection of ailments in preclinical stages, which allows earlier treatment while the disease is still in an infantile stage and potentially

poses a lesser threat to an individual [24]. Screening for disease biomarkers is common practice and is used in the detection of many illnesses such as Alzheimer's disease [24], diabetes and kidney disease [6], and several other neurological disorders [24].

For any biomarker to be considered for use, it must be able to provide relevant information in a consistent manner. The applicability of information supplied by biomarkers is crucial as the information must provide valuable indicators or results for future steps to be taken. Otherwise, the biomarker provides no advantage in disease detection. The repeatability of results is also decisive in the incorporation of a biomarker into PoC tools. Producing false positives is a concern since that generates misleading conclusions which can prove to be harmful where medication would be supplied [25].

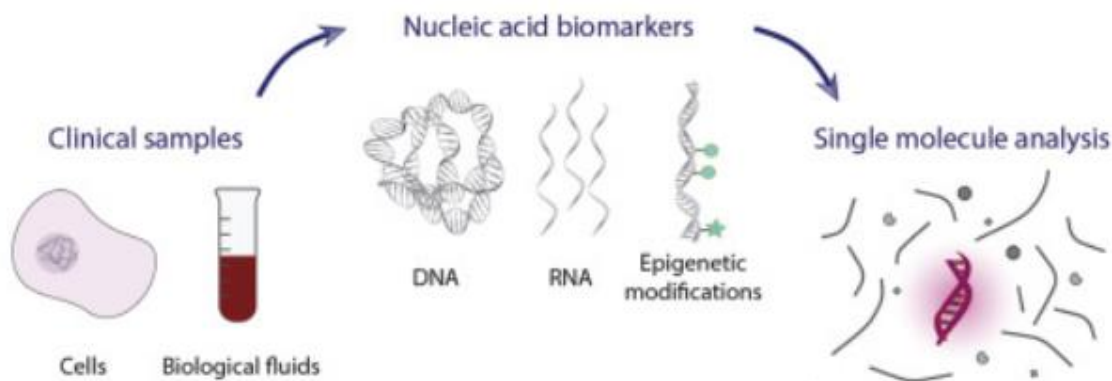


Figure 7: Extraction of biomarkers from biological samples for analysis [26].

Reprinted from Analytica Chimica Acta, Volume 1115, Tal Gilboa, Padric M. Garden, Limor Cohen, Single-molecule analysis of nucleic acid biomarkers – A review, Page 1, Copyright (2020), with permission from Elsevier.

One classification of biomarkers that is critical in disease detection and risk assessment is nucleic acids [26]. The primary biomarkers encompassed by nucleic acids are DNA and RNA structures. Nucleic acids are crucial because they are responsible for containing all the information involved in gene expression. Both DNA and RNA are responsible for the creation of proteins in the body. The information contained within their

makeup can be used in a variety of ways as biomarkers. They can be observed to scan for abnormalities in gene sequences or to identify foreign nucleic acids belonging to other organisms or viruses [26]. There currently exist an extensive quantity of methods for the detection and applying DNA and RNA as a biomarker. This includes sequence recognition, where a set order of nucleotides in a specified order is built on a probe to capture the complementary strand of the target nucleic acid [27]. Other methods include labeling probes as previously described, where fluorophores or quantum dots can be attached to the nucleic acid [27]. Once bound to the target strand or cleaved by a CRISPR system, the fluorescent particle is released from a quencher and emits a detectable signal in a fluorometer. The quenching particle is responsible for suppressing the signal released by the fluorophore while still bound to the probe in close proximity to the fluorophore.

PCR techniques are commonly referred to as the gold standard in nucleic acid analysis since it is capable of detecting single nucleotides in extremely dilute solutions [27]. As previously stated, PCR systems are molecular diagnostic tools used to replicate sequences of nucleic acid in the presence of an enzyme. PCR systems function in three steps. First, the dsDNA is denatured at a high temperature forming two ssDNA molecules [28]. Following the denaturing process, one oligonucleotide primer binds to each strand adjacent to the target sequence through an annealing step [28]. Finally, the DNA polymerase enzyme binds the corresponding nucleotides to the free locations on the ssDNA bordering the primer until two complete dsDNA molecules exist [28]. This process can be cycled and repeated for an exponential replication of DNA strands. Amplification in the number of nucleic acids creates more biomarkers of identical composition making SNV easier to detect or providing a larger sample for use in a less sensitive system. Reverse

transcription PCR (RT-PCR) is a variation on PCR techniques, employing messenger RNA (mRNA) instead of dsDNA for the PCR amplification [29]. Instead of denaturing DNA strands, the mRNA undergoes synthesis of a cDNA strand in the presence of an enzyme and a single oligonucleotide primer [30]. The enzyme named reverse transcriptase, is responsible for the construction of the cDNA onto the RNA starting at the bound primer. Primers can vary in structure from non-specific to gene-specific in their binding sites. A nonspecific primer offers the advantage of being able to amplify multiple mRNA strands in the same solution since the primer is able to adjust nucleotides to match the RNA sequencing [30]. The gene-specific primer is valuable for its ability to increase the specificity of the amplified strand and decrease systematic noise that can arise from variations in mRNA sequencing in solution [30]. One popular improvement made to PCR methods is quantitative or real-time PCR (qPCR). In qPCR, fluorescent dyes are added to solution, which have an affinity for binding to dsDNA resulting from hybridization with the target sequence [26]. Therefore, with the amplification of the target sequences, more hybrids will form and the number of binding sites for the dyes will increase, producing a signal with greater intensity over time [26]. Quantitative RT-PCR (qRT-PCR) has an identical process to RT-PCR with the addition of fluorescent dyes onto the RNA molecules on the end opposing that of the primer [26]. Once the enzyme begins building the cDNA, the fluorescent dye will be cut from the RNA strand, freeing the dye from the quencher, and releasing a detectable signal [30]. As more probes are broken the strength of the signal increases in intensity allowing for real-time monitoring of the amplification and PCR. The process of qPCR and qRT-PCR are only able to be used as semi-quantitative due to the

amplification bias that can occur through SNV in PCR techniques [26]. Still, the qPCR technique has become known to be the gold standard for nucleic acid analysis.

2.2 Use of PoC Systems for NAT

Regardless of PCR systems being the gold standard for NAT, they are inefficient for use in PoC devices. This is due to the bulky nature of current tools and the required sample preparation before testing for current methods. The complexity and resource requirements limit where PCR-based techniques can be employed, namely centralized laboratories or hospitals with proper equipment and personnel [31]. The reaction demands a comprehensive understanding of the process at all three phases: sample preparation, denaturation and amplification, and detection. Sample preparation is crucial in the efficiency of PCR and demands time and resources to isolate nucleic acids. PoC systems trying to utilize PCR often require high concentrations of starting material which can be hard to obtain, especially for dilute biomarkers [32]. They are also highly susceptible to false positives and negatives due to improper sample preparation. Most preparation techniques are manually performed allowing for more errors and contaminants to limit the amplification and detection of the target sequences. Contaminants have the possibility to function as inhibitors that constrain the polymerase, or other enzymes used, in the construction of complementary molecules on the mRNA or ssDNA [31]. In RT-PCR, the isolation of RNA can prove difficult. RNA can be sensitive to changes in pH affecting the concentration of the resulting nucleic acid sample [30]. Amplification poses a challenge in PCR along with sample preparation. As target sequences get amplified, so do errors or mutations hidden within the segment. In qPCR, variations in the number of unique DNA sequences can cause a fluorescent signal to vary in intensity resulting from improper

cleavage of probes, therefore misrepresenting the actual quantity of copies made by the reaction [30].

In order to improve upon PCR for integration into microfluids, isothermal amplification was employed as an alternate PoC device. It was more compact and offered a cheaper alternative without the addition of heating [31]. This opened the possibility for PCR to be used on PoC devices in combination with new detection methods. Isothermal amplification still had drawbacks making alternative methods favorable in microfluid analysis. Extensive sample preparation is still required before introduction to the system. At isothermal conditions, the limit of detection (LOD) is too high with some methods causing poor sensitivity [33]. To be able to use this new method for NAT, advancements need to be made in improving the reliability of results and the integration of all aspects into a single, portable device.

Other technologies for NAT in PoC devices include bioluminescence amplification [34, 35, 36], probe-based assays [34, 35, 37], or electrochemical microarrays [38, 39]. These techniques are often categorized based on their detection method. The groupings include hybridization assays, sequence-based testing, and trapping methods, with many of these techniques combining aspects of multiple categories [35]. Bioluminescence or fluorescence is commonly used in a multitude of systems, as it provides quantitative and real-time updates on the status of a device. This allows for a higher sensitivity in testing and a reduction in the size of micro assays [36]. Probe-based assays work by immobilizing a single-stranded oligonucleotide chain, typically ending with a label or fluorescent dye, onto a device substrate or nanostructure [34]. These probes then hybridize in the presence of the target nucleic acid and produce a detectable signal based on the label utilized. DNA

probes are often used in conjunction with other techniques, such as amplification since the probes are highly customizable. The blending of probe-based assays allows for PoC devices with higher sensitivity and lower detection limits than ordinary hybridization tools. As shown by Yang et al. in **Figure 8**, utilizing an enzyme capable of facilitating recycling amplification in the presence of a target sequence that then hybridizes with a fluorescent probe, provides a highly sensitive system that is capable of producing rapid results in real-time [37]. This is one use for fluorescent probes in detection.

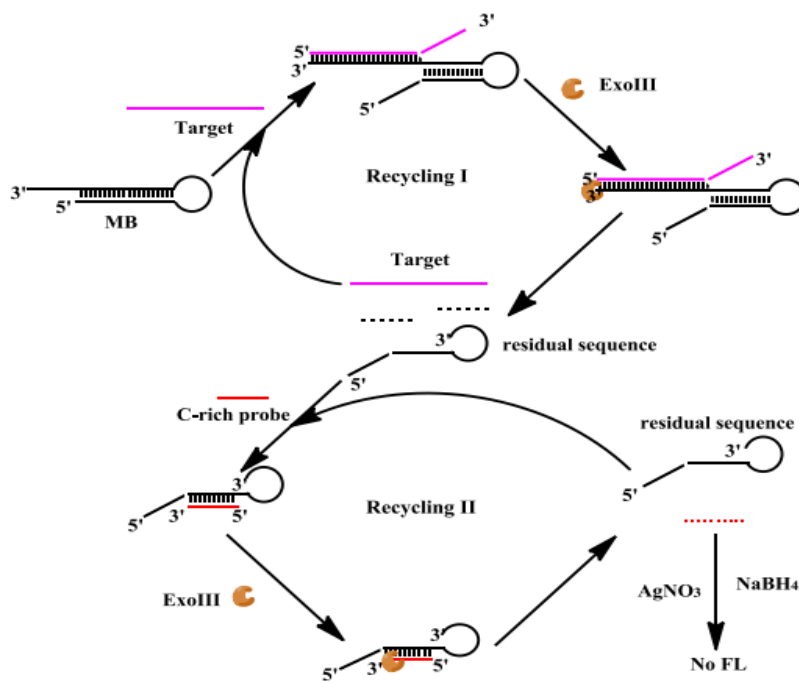


Figure 8: Process described for recycling amplification for nucleic acid testing [37].

Reprinted from Analytica Chimica Acta, Vol 900, Yang et al., A label-free fluorescent probe based on DNA-templated silver nanoclusters and exonuclease III-assisted recycling amplification detection of nucleic acid, Copyright (2015), with permission from Elsevier.

Alternatively, probe assays can be used in electrochemical systems instead of in combination with amplification methods. Devices that employ electrochemical systems are highly sensitive causing an increased efficiency in sample detection. Through the immobilization of DNA probes on the surface of a transducer, an electrical signal is produced indicating the presence of the target strand [38]. Once the DNA duplex is formed between the probe and target sequence, electroactive indicators bind producing an increased current signal. The indicators are commonly used alongside enzyme or redox labels that preferentially bind to the target strand over the ssDNA probe [38]. For these systems, the surface condition is crucial. The density or packing of the probes onto the substrate or nanoparticles can affect the selectivity of DNA binding and minimize non-specific adsorption [38, 39]. Single-base mismatches can be detected through proper selection of the probe. It has been shown that peptide nucleic acids (PNA) provided higher sensitivity in a biosensor when compared to certain ssDNA probes [40]. As well as being a label-free detection method that does not require amplification [40]. PNA probes are often used for single-base mismatch screening due to the instability of PNA and target DNA hybrids when compared to DNA probes and target hybrids [39]. Therefore, in the presence of a mutation, a stronger signal is produced since the PNA/DNA target hybrid

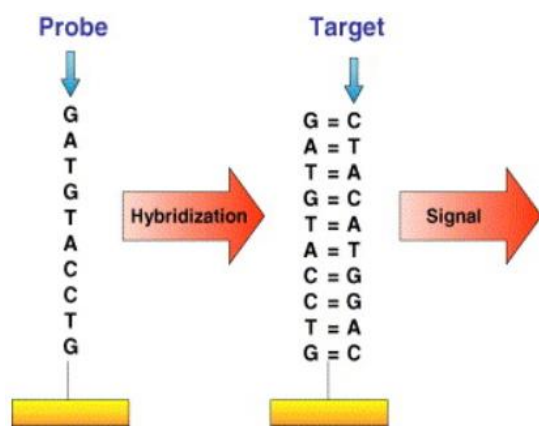


Figure 9: Changes in surface condition on a transducer following hybridization for detection of a target [38].

Reprinted from Biosensors and Bioelectronics, Volume 21, Joseph Wang, Electrochemical biosensors: Towards point-of-care cancer diagnostics, Page 2, Copyright 2005, with permission from Elsevier.

will degrade which implies the mismatching base pair is present. This is key to the early detection of diseases like cancers, which are caused by genetic mutations [38].

2.3 Role of LSPR in PoC Devices

Incorporating nano-biosensors into PoC devices gives the advantage of real-time detection of nucleic acids. LSPR systems offer an advantageous alternative to previous detection methods such as electrochemical and qPCR techniques. The integration of nanoparticles smaller than the incident light wavelength as the main component for detection allows for the miniaturization of PoC devices. This allows for higher portability of devices used for on-site testing. Compared to many PCR tools that require large-scale equipment and a centralized testing lab, LSPR devices offer a quick turnaround after experimenting. The advantage of LSPR techniques in PoC devices relies on four principles [41]. One of the core principles for PoC devices with LSPR systems is the ultrahigh sensitivity in screening caused by the changes in the RI. Relying on the interactions between light and metallic nanostructures, the dielectric properties surrounding the particles vary with their environment [41]. The other principles include the specific detection of target analytes, the integration of sample treatment and analysis, as well as the portability, automation, and ease-of-use help to make a portable PoC device [41]. Automation in PoC is aided by the miniaturization of the LSPR detection system. The less area required for detection allows for more space to be allotted for microfluid separation, a common issue with PoC testing. Designing a device capable of autonomously separating target analytes from the rest of the sample eliminates human error from sample preparation [42]. Plasmonic systems provide a simpler method in preparation due to the ability for label-free detection of nucleic acids which simplifies the preparation to only isolation of

nucleic acids in most cases. Detection of the target analyte is simplified by LSPR where only two measurements are required. By comparing a baseline spectrum of the nanoparticles to a spectrum after the addition of the sample, detection of single molecules or nucleic acids can be observed. Incorporating the LSPR technique, the intensity of the resulting electric field is enhanced at the plasmonic resonance frequency, making minimal peaks more pronounced above the noise [43]. Due to the shift in the RI by the binding of target analytes to the surface of the nanoparticles, a red or blue shift in the peak of the spectrum can be observed [44]. Devices employing LSPR substrates are made possible by portable spectrometers, which allow for PoC devices to be more portable [42]. LSPR systems also have the advantage of being insensitive to minor changes in the angle of incidence of light since the light is directly interacting directly with the sample [42]. This is in contrast to SPR methods, where the incident angle off the metallic film is controlled and adjusted to ensure the greatest resonant signal [44].

Due to the growing interest in LSPR for PoC devices, distinct characteristics need to be adjusted for specific sequences. For different applications, the nanoparticles used can be constructed in different arrangements and densities. This can affect the RI sensitivity, the surface decay length, the number of non-specific bindings, and the plasmon resonant frequency that results [43]. Coinage metals are typically used for nanostructures, primarily gold and silver due to their resonant wavelengths in the visible region. Copper and aluminum are alternative metals to gold and silver that have been investigated for their abilities in LSPR sensors [45]. They are often avoided due to their susceptibility to oxide formation [45]. Silver offers higher intensities and sharper peaks in spectrum displays than gold structures would [45]. However, gold is still the common metal used since it has

greater chemical stability in nanoparticles for nucleic acid detection when compared to silver particles [45]. Nanoparticles made from gold and silver can be fabricated in a number of ways. Nanoparticle systems are typically in the form of a colloid, where the particles are suspended in a liquid, or in the form of printed structures onto a substrate. There are many lithography procedures and ion beam techniques, or chemical reactions from both organic and inorganic reactants to form the nanostructures and colloids respectively [45, 46].

Suspended nanoparticles are often formed through reduction reactions, producing a high volume of particles at a low cost [43, 45, 46, 47]. Techniques employing chemical reactions to produce nanoparticles are often referred to as a bottom-up approach, where the conditions and dimensions of the nanoparticles are determined by the reaction [45]. Typically, gold chloride is dissolved in water with a reducing chemical such as phosphorus [46]. Synthesis by this method often requires stabilizing agents to prevent the nanoparticles from aggregating and precipitating out of solution [48]. The stabilizers limit the van der Waal's forces between the nanoparticles and help to prevent oxidation [48]. Citrate is a common example of stabilizers used for producing colloidal gold or silver. A number of other wet-chemistry combinations are possible in synthesis of nanoparticles. Other than reduction reactions, biological reactions have been shown to be able to produce inorganic nanoparticles. Biological synthesis provides a nontoxic alternative to the synthesis of particles through the use of algae, bacteria, and even some viruses [47]. These organisms and viruses required controlled environments to operate in most cases, needing specific pH values and temperatures to ensure the proper formation of nanoparticles [47]. Often neutral pH values and ambient temperature conditions were sufficient for the reactions. The

drawback to the nontoxic reactions is the formation time, which can range from one day to five days for bacteria and fungi [47].

Both methods for colloidal metals can be altered to form a wide variety of shapes, the simplest being a sphere. Most shapes are possible for nanoparticles, however nanospheres, rods, shells, triangles, cubes, and stars are common configurations [46, 47]. Producing nanospheres is the easiest shape to achieve as it occurs naturally from wet-chemistry. In one method to achieve the other shapes, micelles or hard templates as shown in **Figure 10**, are formed to control and achieve the desired AuNP shapes from seeded growth [48]. These molds are often used in the formation of nanorods [49]. To best control the aspect ratio of nanorods, spherical nanoparticles are often planted inside the templates

to act as seed for promoting growth the rod [49]. The process of using spherical shapes to grow varying nanostructures is referred to as seeded growth and can provide more reproducible and exact shapes compared to one-step growth [45]. The advantage of hard templates allows for tighter control on the size, while being adjustable for new lengths. Micelles provide the better option for a larger scale-up at the cost of weaker control on aspect ratio [49]. Colloidal gold and silver can be adjusted for a variety of applications with the numerous methods for formation and the

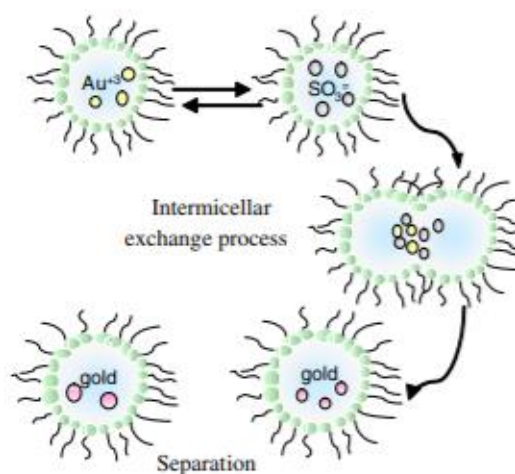


Figure 10: Demonstration of the formation of gold nanoparticles through micellar exchange [48].

Republished with permission of Nanotechnology, Volume 16, from Herrera et al., Synthesis and agglomeration of gold nanoparticles in reverse micelles, Page 3, Copyright 2005; Permission conveyed through Copyright Clearance Center, Inc.

diverse configurations available making it a well-suited biosensing method for PoC devices.

Construction of nanoparticles onto a substrate is an alternative method to suspending nanoparticles in solution for LSPR detection. Methods for fabricating nanostructures onto solid supports are referred to as top down techniques since the structures are often chemically bound to the surface of a substrate [45]. Top down assembly is better suited for creating larger quantities of samples by the nature of techniques used [23]. Commonly used techniques included electron beam lithography (EBL) or focused ion beam (FIB) etching and deposition [45]. These two techniques are highly advanced and produce specific nanostructures that might not be possible in colloids such as nanodisks, rings, and holes [45]. The techniques are expensive and limit the number of commercial locations able to produce samples. Other techniques for lithography are possible such as silanization, where metallic nanoparticles are immobilized onto the surface of a glass substrate, offer cheaper alternatives to EBL and FIB tools [45]. Silanization is the process in which a monolayer is formed on the surface of glass or silicon oxides which allows for the binding of the metallic nanoparticles [50]. The substrate needs to be free of contaminants for proper monolayer formation such that the hydroxyl groups are exposed, and the monolayer can form [50]. This method has poor control over the density and spatial distribution when compared to lithography and ion beam techniques but offers a simpler and cheaper alternative for situations where packing dimensions might not be tightly controlled.

New techniques combining both bottom up and top down approaches have received significant interest in developing high-resolution nanostructures onto a substrate for LSPR

biosensing. Combining both of these methods can limit the time consuming steps, such as lithography, but maintain high accuracy and reproducibility. Etching techniques take advantage of specific chemistries for the removal of coatings on a substrate that result from lithography. Wet and dry etching methods show the capability to produce complex nanostructures in pillar-like formations [23, 43]. Gold nanoparticles are used as a mask on a silicon dioxide layer and prevent etching directly below them. Nanoislands or nanodisks are common nanoparticles created for masks and act as caps protecting the layer below from removal. The addition of an aggressive gas or liquid, such as sulfur hexafluoride, will selectively remove silicon dioxide where the gold nanoparticles are not present resulting in the pillar-like structures [23]. This creates mushroom-like features from the gold caps with the silicon dioxide as the stem on a glass substrate. These nanomushrooms have been shown to have extremely low limits of detection near 66 zM [23]. It has also been shown that the nanostructures help to reduce nonspecific binding of DNA targets by 41% through separation of the electromagnetic field of the substrate and the plasmonic structures [45]. These nanomushrooms provide a compact detection method suitable to fit into PoC devices. The low limit of detection and high sensitivity to single molecule binding provide a promising mobile device since small-scale and portable optical spectroscopy methods can be employed for detection. As well as the ability for label-free detection, which further simplifies a PoC device utilizing LSPR nanostructures.

2.4 Employing CRISPR for Sensing Methodologies

The role of CRISPR/Cas complexes in PoC devices provides a similar advantage to LSPR biosensing. Comparable to how LSPR techniques can detect analyte samples with single molecule sensitivity, CRISPR tools have the sensitivity to detect single base-pairs

within a molecule of DNA. These systems offer rapid, low-cost testing of samples containing attomolar quantities of target strands with ultrasensitivity [51]. Due to the variety of Cas systems that exist and the customizability of CRISPR molecules, CRISPR/Cas systems provide versatile NAT in PoC devices by being able to detect both DNA and RNA from a variety of readout methods [51, 52]. Common detection methods for CRISPR biosensing devices include colorimetric [51, 52, 53, 54], electrochemical [51, 52, 53], and fluorescent detection tools [51, 52, 53, 55]. These varying readout possibilities increase the versatility and widespread use of CRISPR systems in PoC applications.

Electrochemical detection is well suited for use in CRISPR biosensing devices for its ability to detect dilute samples without the need for amplification processes such as PCR [51, 52]. As previously stated, a form of transistor is required to produce an electric signal in response to a change in the surface condition of the transistor [38]. A common design for electrochemical sensing is to use graphene field effect transistors [51, 53]. These structures can immobilize dCas9, which has both nuclease domains deactivated, preventing the CRISPR tool from cleaving target DNA strands [53]. As a result of the Cas9 complex being deactivated, the CRISPR binds with the target DNA instead of cleaving it, causing an increased concentration of charged molecules on the surface of the graphene, which decreases the resistance of the system and changes the electrical signal obtained [53]. Systems utilizing the cleavage ability also exist where DNA strands labeled with reporter molecules are immobilized onto the surface of a transistor [51, 53]. Introducing CRISPR systems to the surface, the target strands will be cleaved resulting in a separation or destruction of the reporter component which affects the electrical output.

The use of colorimetric detection is popular alternative to an electrochemical method due to its widespread accessibility [53]. This method of detection relies on a visible change in color when exposed to a target analyte in the sample. For CRISPR samples this can be used to identify particular sequences of interest [53]. Samples incorporating colorimetric detection are often simple, easy-to-use devices that allow for broad application and robust testing [52]. Pregnancy tests are common examples of colorimetric detection, which employ lateral flow assays (LFA), instead of CRISPR systems, that immobilize target antigens onto antibodies, resulting in a visible color change [52, 54]. Other than LFAs, colorimetric detection can be easily employed in nanoparticle systems since gold nanoparticles in solution undergo a color change when aggregating together [54]. This detection method makes up the majority of commercial PoC systems available because these assays can offer rapid testing in portable devices at a low cost. The shortcoming of colorimetric systems is that they provide only qualitative responses from the resulting color change, or the absence of one. In some cases, the intensity of the resulting color can provide limited quantitative information, but that can be hard to measure and often require additional detection methods to obtain valuable information.

Fluorescent detection methods work well in conjunction with CRISPR/Cas systems for use in PoC devices. As shown in PCR technologies, the use of fluorescent particles can allow for real-time detection and both qualitative and quantitative results, making them

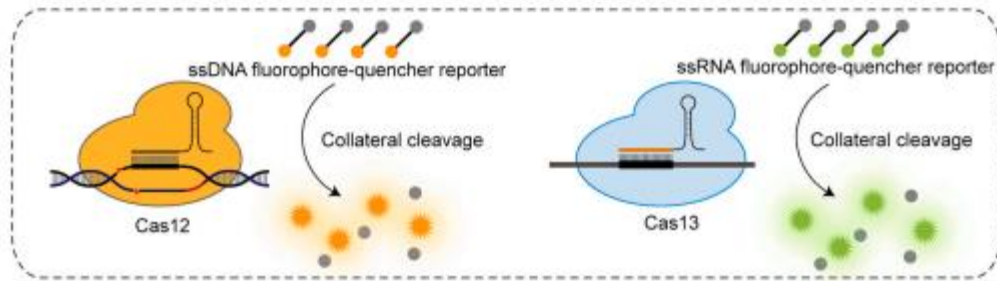


Figure 11: Demonstration for fluorescent detection by Cas12 and Cas13 cleavage [51].

Reprinted from Biosensors and Bioelectronics, Volume 165, Wang et al., CRISPR/cas systems redefine nucleic acid detection: Principles and methods, Page 2, Copyright (2020), with permission from Elsevier.

desirable for use in PoC tests [34, 36]. Instead of amplification in PCR devices, early CRISPR complexes incorporated fluorescence as shown in **Figure 11** to detect the presence of specific target sequences in DNA or RNA molecules [51]. One example system is SHERLOCK, where fluorescence was achieved through quencher-labeled reporter nucleotides that released a fluorophore following target binding by the Cas13a protein [52, 55]. This process allowed for signal amplification rivaling PCR processing at 10,000 times greater than the original intensity, due to the adjacent cleavage ability of Cas13a and other proteins such as Cas12 [17, 21, 53, 55]. The collateral cleavage in the presence of a target sequence creates further degradation of the quencher probe, which causes higher turnover in the target molecules [55]. This eliminates the need for amplification methods such as PCR or isothermal amplification and will simplify point of care devices. Since the use of fluorescence in combination with CRISPR systems drastically amplifies output signals, detection of ultra-dilute samples becomes possible, making them practical choices to be incorporated into PoC devices [52]. Fluorescent biosensing is often desirable in testing dilute samples since fluorometers offer background-free detection, which aids in

amplifying the signal-to-noise ratio and the already enhanced output signals that resulted from cleavage [53]. This variety of sensing methodologies makes CRISPR a versatile tool, capable of combining with other powerful tools such as LSPR. Introducing Cas proteins to the surface of LSPR nanostructures takes advantage of the high customizability of CRISPR complexes and the enhancement capability of the nanoparticles, resulting in a highly sensitive and accurate system for nucleic acid detection. This method also offers a label-free detection method that provides the advantage of simplifying the required sample preparation.

3.0 Fabrication of Microfluidic Cell

3.1 Development of the AuNM substrate

For the label-free capture of AuNPs, a unique system was fabricated. This AuNM substrate was created using multiple microfabrication techniques [23]. These nanoscale geometries were constructed on a SiO₂ substrate that was pretreated with acetone and

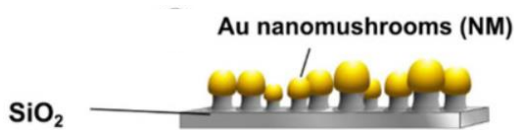


Figure 12: 3-D schematic highlighting AuNM components [23].

isopropanol. To this surface, a thin Au film was deposited at a thickness of 4 nm using electron beam vapor deposition (KE604TT1-TKF1, Kawasaki Science) [23]. This was done at a rate of $0.1 - 0.2 \text{ \AA s}^{-1}$. The film then underwent an annealing process at a temperature of 560°C for three hours, which caused the film to form randomly dispersed Au nanoislands (AuNIs) across the SiO₂ layer [23]. These AuNIs function as the cap of the AuNMs and enable the use of LSPR as opposed to SPR enhancement since the AuNI is similar to that of a nanosphere. The annealing process has another function in anchoring the new particles into the surface of the SiO₂ which helps to prevent liftoff during later fabrication processing, as well as experimentation. Following the annealing process, the exposed SiO₂ was removed by reactive ion etching (RIE) with SF₆ gas flowing at a rate of 45 sccm and 10 mTorr (Plasmalab 100, Oxford Instruments) [23]. This gas selectively etched off the SiO₂ while ignoring the gold component, leaving only the substrate directly underneath the anchored AuNIs remaining. The resulting structures

isopropanol. To this surface, a thin Au film was deposited at a thickness of 4 nm using electron beam vapor deposition (KE604TT1-TKF1, Kawasaki Science) [23]. This was done

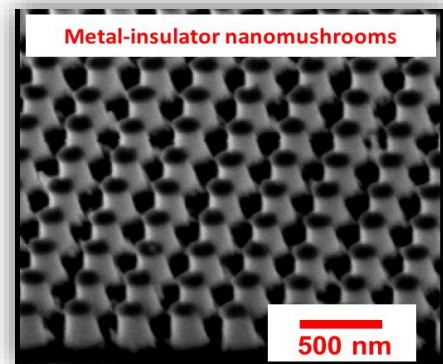


Figure 13: SEM image of nanomushrooms [23].

formed the stems for the AuNMs that can be seen in **Figure 13**. The unique geometry allowed for highly sensitive LSPR detection across the surface. Using a nanosphere-like structure provided a greater area of conjugation for the additional AuNPs to adhere, while the solid stem adhered to the sphere to create a robust physical device. Other methods for periodic AuNM fabrication were reported using electron beam lithography to form AuNI arrays, but for this work randomly-ordered structures sufficed [23]. Future experimentation could lead to the incorporation of the ordered structures for more sectional testing.

3.2 Forming the PDMS device

The AuNM substrate mentioned above was sealed within a microfluidic chamber comprised of a polydimethylsiloxane (PDMS) mold which was adhered to a common glass slide. The combination of both components provided a vessel capable of containing solutions for surface treatments onto the AuNMs. For the formation of the PDMS component, a silicon elastomer base was mixed with a curing agent (SYLGARD 184) in a 10:1 ratio and was slowly poured over a 3-D printed resin mold that had been placed in a 90 mm glass petri dish. The resin mold used was prepared via 3-D printing (Form2, Formlabs) and was used to create a square cutout in the PDMS. This square was 2.2 x 2.2 x 4 cm in order to house the AuNM chip that was 2 x 2 cm, while allowing for space above the substrate for fluid flow. After covering the resin mold in the PDMS solution, the petri dish was placed under vacuum for 30 minutes to ensure there were minimal air bubbles trapped within the PDMS, as this could create cavities and affect the performance of the microfluidic cell later on. The petri dish was relocated to an oven after the vacuum, where it was exposed to 75°C heat for approximately five hours. This step was originally performed at 100°C for one hour, but at higher temperatures the resin began to warp which

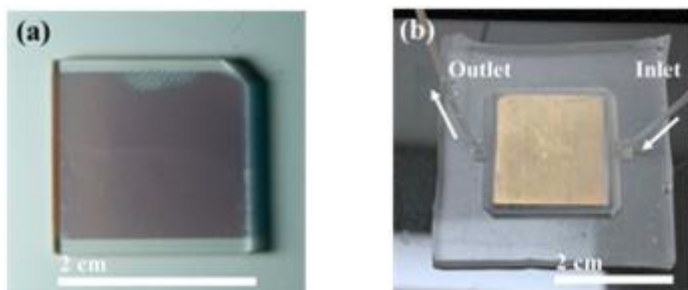


Figure 14: Images of the a) AuNM substrate and b) constructed microfluidic cell.

affected the quality of the PDMS-glass seal for all future samples. Following the oven treatment, the PDMS was cut from around the ultrasonic bath. The cleanings were performed at room temperature for five minutes in two different passes; once in a solution of acetone, followed by a 50/50 ethanol and deionized (DI) water mixture. Into the square cutout on the PDMS layer, two 1 mm holes were punched into opposing corners. These holes were fitted with 10 cm long, 1 mm diameter surgical tubing, which is visible in **Figure 14** as the inlet and outlet. A syringe was fitted into the tubing and used to control the inlet and outlet fluid flow. During the course of early experimentation, leakage was quite common between the PDMS shell and glass slide. These events would cause substantial portions of the sample solution to be wasted, affecting results. To combat this, the surface of the glass slide and the PDMS layer were exposed to an oxygen plasma which created hydroxyl groups on the surface that aided in creating a fluid-tight seal between the two components. Following this, extra PDMS was occasionally cured along the contact point between the layers to further aid in creating the seal. In order to keep the AuNM substrate adhered to the glass slide, a 2 x 2 cm portion of double-sided tape was cut and added to the plasma-exposed glass slide. It was important to ensure that nothing came into contact with the topside of the AuNM as it was being placed onto the tape so that the nano-geometries remained intact. At this point, the PDMS mold was placed over the AuNM chip and onto the glass slide. The total cell was placed onto a hot plate at 125°C overnight to seal the PDMS to the glass

slide. The end result was a liquid-tight chamber with a total volume of 240 μL that was able to hold the test fluids and the AuNM substrate.

4.0 Optimization of Surface Binding

4.1 Preparation of Reagents

For this work, streptavidin-coated 40 nm AuNPs (nanoComposix Inc.) suspended in 1.0x PBS, 0.5% BSA, 0.05% Azide were used for most experiments. Other tests incorporated bare (citrate-coated) AuNPs with diameters ranging from 4 – 200 nm and concentrations varying from 0.115 nM to 9.26 μ M. These solutions were all adjusted to 1.1 nM before being added to the device, unless otherwise stated. The bare 40 nm AuNPs (nanoCompsix Inc.) were suspended in an aqueous 0.02 mM sodium citrate solvent, while the 4 nm, 100nm, and 200 nm nanoparticles (Luna Nanotech) were suspended in water with 0.01% Tween-20. In some later experiments, the bare 40 nm particles were extracted from the citrate solutions and resuspended in DI water through a solvent exchange process. This was done for a 10 μ L sample placed in a centrifuge at 1500g for 45 minutes, as recommended by nanoComposix Inc. The supernatant solution was then removed and replaced with an identical quantity of nuclease-free water (NFW). To resuspend the particles, the vial was vortexed until the aggregate particles disappeared.

4.2 Early Protocols

The initial design for this work was to form AuNP-AuNM couples that were linked with a DNA strand that could then be cleaved by CRISPR-Cas12a proteins. This protocol was a newer single-step binding protocol developed to link two AuNPs but was altered for our system [56]. To achieve this, 240 μ L of poly (A)-tagged DNA probes were added to the surface of the substrate before being immediately exposed to a -20 $^{\circ}$ C freezer for 70 minutes. After the device thaws, the surface was washed with 730 μ L of PBS buffer three times. The washings were performed to ensure the removal of any unbound probes or other

material from the surface to certify later measurements were accurate to the actual conditions on the AuNMs. This washing protocol was refined in later iterations for forming the AuNP-AuNM couple by adding a syringe pump (SP2201 World Precision Instruments) that controlled the flow rate of PBS. A faster speed would have the potential to dislodge weakly bound components, altering the results, instead of simply removing unbound probes. For this DNA linkage protocol, the DNA was first labeled with fluorescein amidites (FAM) dyes instead of a biotin linker. Therefore, the fluorescent intensity of the washing solutions was able to be tested to observe a decrease in intensity as a way of verifying the binding of the probes to the AuNM structures. This was shown in **Figure 15** where after the first wash with PBS, the second and third wash had a fluorescent intensity comparable to that of a blank cuvette. Even the fluorescent intensity of the first wash was less than one-tenth of the initial DNA probe solution, indicating that the binding protocol was effective for DNA. In **Figure S2** the intensity of the pure DNA probe solution can be seen with a fluorescent intensity around 10,000 units compared to the washing solutions shown here.

After this confirmation, the AuNPs were added according to the protocol to construct the AuNP-DNA-AuNM link. A similar biotinylated-DNA strand was used to bind to the streptavidin coating of the AuNPs. To a 20 μL sample of AuNPs, 5 μL of 1 μM biotinylated-DNA was added in an

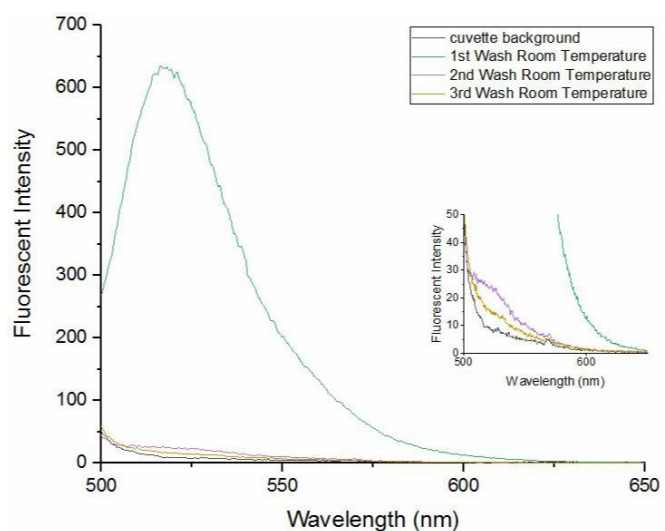


Figure 15: *Fluorescent spectra for three washes of FAM-DNA probes.*

off-chip tube and mixed. This ratio was based on the approximate number of binding sites within the streptavidin molecules on the surface of the nanoparticles, as reported by nanoComposix Inc. The resulting solution was added to the microfluidic cell and incubated and washed following the procedure mentioned above. After the washing step, the AuNMs were removed from the PDMS shell and double-sided tape and allowed to air-dry overnight in a covered petri dish. This was done to evaporate any remaining solution that could alter the local RI surrounding the unique structures. Comparing the absorption spectra of the substrate before and after the addition of the AuNP-DNA complex exhibited a large redshift in the peak wavelength value. For further confirmation of the construction of the coupling, the same protocol was run without the DNA linker. To our surprise, the resulting absorption spectra produced a near identical redshift, implying that the AuNPs were nonspecifically binding to the AuNM without the need for a linking component.

The nonspecific formation of the AuNP-AuNM couple was originally combatted by changing the protocol to a more established salt aging method previously used to form AuNP aggregates [57]. For this method, 10 μL of AuNPs were added to 2.5 μL of tris(2-carboxyethyl)phosphine (TCEP) along with 2.5 μL of the 1 μM biotinylated-DNA. The volumes were halved to allow room for the TCEP, and NaCl solutions later. The TCEP molecule has a high binding affinity for gold, which would help coat the exposed portions of the AuNP and prevent aggregation with the AuNM. The solution was incubated for two hours at room temperature before being mixed with 135 μL of NFW. The new solution was incubated on-chip for twelve hours at room temperature. After this, 20 μL of NaCl solution was added once each hour for five hours, followed by a ten second sonication. The salt solution was added to neutralize the charge of the system in hopes of preventing

aggregation of the AuNPs. This procedure can be found in more detail in section 9.3 of this work along with other supplementary information. The final cell was wrapped in parafilm to prevent evaporation and set aside for 24 hours before following the previously mentioned washing and measurement procedure. It was observed that without the parafilm, NaCl solution would flow out of the inlet and outlet holes due to capillary action. The results of the salt-aging protocol showed comparable results to that of the single-step binding, where the AuNPs directly couple with the AuNM surface which was undesirable at the time.

A final protocol was developed that employed thiol-binding to link the AuNP to the substrate. This procedure can be seen in section 9.3 along with the supplementary information at the conclusion of this work. The new approach expanded upon the salt-aging procedure previously discussed but employed biotin-ssDNA-thiol modified probes as opposed to the normal biotinylated-DNA [58]. The probes were designed following the thiol strands used in common literature [58]. For forming the AuNP-AuNM couple, the thiol group was added to preferentially bind to the AuNM while the biotin would bind to the streptavidin coating on the AuNPs. The new variation on the binding protocol still resulted in the same conclusion as the two previous protocols where the AuNPs would bind onto the AuNM regardless of the DNA presence. The three methods above failed to develop the AuNP-DNA-AuNM coupling that was initially desired for CRISPR cleavage. This failure led to further investigation of the AuNP aggregation on the AuNM structures which required a new direct addition protocol to investigate the effects.

4.3 Direct Addition Protocol

After observing the large-scale redshift produced by the addition of the AuNPs, the project changed direction to investigate this phenomenon further. For this, a new direct addition protocol was developed for the formation of a linker-free AuNP-AuNM couple. This procedure is described in detail in section 9.4. In the first version of this method, 7 μL of AuNPs were conjugated with 0.5 μL of 100 μM FAM-DNA-biotin for 30 minutes on a shaker before being added to the microfluidic cell. The DNA was used to link the AuNPs to other components in various applications, making the system customizable. The effect of the DNA strands on the detected redshift was evaluated by applying a solution containing only the ssDNA, with no statistically significant shift detected. Therefore, if the DNA was to be omitted from the test, 7.5 μL of AuNPs were diluted

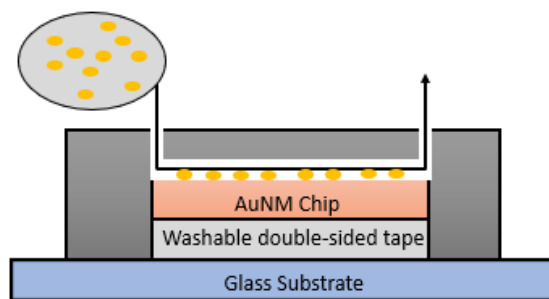


Figure 16: Diagram for the addition of AuNPs to the microfluidic cell.

in 222 μL of NFW before finally being added to the AuNM surface which was subsequently wrapped in parafilm to prevent further evaporation or contamination during incubation. The solution was allowed to rest on the surface of the substrate for twelve hours at room temperature before undergoing the original washing procedure with 730 μL of 1x PBS buffer at a rate of 146 $\mu\text{L}/\text{min}$ three times. The system used to measure the absorbance of the surface was custom built for this application and is shown in **Figure S1** and explained in section 9.2. This procedure was adapted for later experiments to include changes in concentration, diameter, and the coating on the AuNPs.

5.0 Analysis of the Surface Condition

The binding of the AuNPs to the surface of the AuNMs caused a change in the local refractive index which resulted in the redshift observed in the peak wavelength for the adsorption spectra. These AuNPs formed clusters surrounding the AuNM which produced strong “hotspots” that provide the resulting LSPR effect. To demonstrate the wavelength delta, the absorption spectra were measured before and after the addition of AuNPs, which resulted in a 30 nm redshift as evident in **Figure 17**. This also resulted in an increased absorbance in samples that had AuNPs (1.1 nM) introduced to the system. All peak resonant delta measurements shown are an average of at least three sites across the surface of the AuNM chip with the appropriate error bars applied.

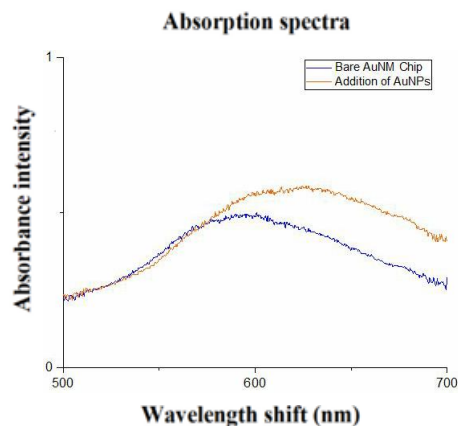


Figure 17: Absorbance spectrum for the observation of the redshift resulting from the addition of AuNPs to the AuNMs.

The capability of the LSPR system was investigated further by measuring the wavelength shift of AuNPs with different diameters ranging from 4 to 200 nm, all with fixed concentrations at 1.1 nM. Based on the results, the 40 nm AuNPs produced the greatest redshift (~30 nm). In contrast, the smaller 4 nm particle produced a minor redshift of ~11 nm. The effects of diameter on the magnitude of the redshift can be seen in **Figure 18** where the 4 and 40 nm particles, as well as the 100 and 200 nm particles, are summarized. For the larger two particles, their addition resulted in a redshift of approximately 25 and 23 nm, for the respective 100 and 200nm AuNPs. These results showed that there was an optimal size constraint on the AuNP-AuNM couple. The smaller

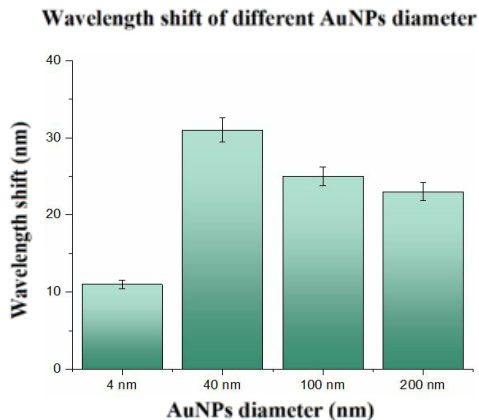


Figure 18: Effect of AuNP diameter on the apparent redshift in resonant wavelength.

particles produced a smaller wavelength shift due to weaker LSPR interactions. The resulting “hotspots” could not produce as strong of an enhancement factor to the incoming photons. It would be expected that the larger AuNPs would produce a larger wavelength delta, but instead resulted in a smaller redshift. This is due to the formation of aggregates which were easily dislodged by the washing procedure. The clusters formed by these two larger particle sizes could be seen visibly aggregating, as well as flowing off the surface of the AuNMs under the forces of the PBS washing.

To further determine the optimal conditions for forming the coupling, the coating on the AuNP was investigated. For this experiment, the streptavidin-coated 40 nm AuNPs were compared to two varieties of bare (citrate-coated) 40 nm AuNPs. The two bare particle samples differed in their carrier solution from a dilute sodium citrate stock solution to a DI water solution. This was done using a carrier exchange procedure suggested by nanoCompSix Inc. as described earlier in section 4.1. For the bare particles, a lesser 9 nm and 12 nm redshift were observed in the respective solutions, while the streptavidin-coated AuNPs produced the 30 nm wavelength

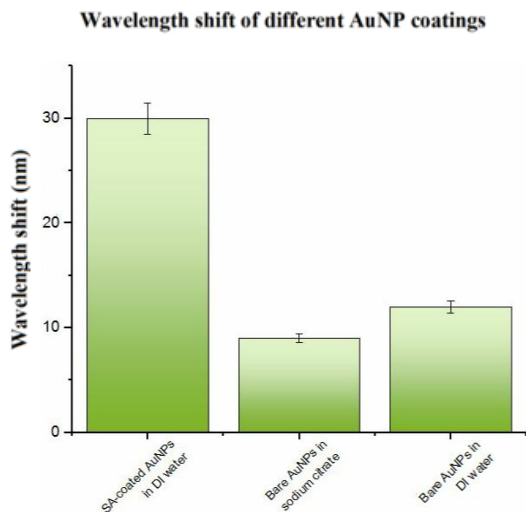


Figure 19: Redshift resulting from variations in AuNP coatings.

shift mentioned previously. These results can be seen in **Figure 19** where the streptavidin AuNPs produced a three times greater redshift. The smaller redshift resulting from the bare AuNPs is due to the presence of the citrate molecules, which are charge neutralizing and used to prevent aggregation of AuNPs while in storage [59]. This would further prevent the formation of aggregates surrounding the AuNMs, which resulted in a weaker wavelength shift. For the bare AuNPs in DI water, there still remained a small fraction of the citrate molecules present as not all the fluid could be exchanged. The citrate molecules also remained weakly adhered to the surface even in the DI water, which further prevented the formation of the desirable aggregates. Since this was a linker-free addition, the citrate molecules were not displaced by anything and left weakly associated. Therefore the 40 nm, streptavidin-coated AuNPs offer the greatest advantage and the highest binding efficiency of all tested samples, resulting in a 30 nm redshift in adsorption peak wavelength value.

A final test was performed to determine the effect of concentration on the microfluidic system. From concentration testing, it was determined that the 30 nm wavelength shift was observable at concentrations greater than 500 pM which can be seen in **Figure 20**. Concentrations including 1000 pM, 750 pM, and 500 pM were tested to verify the maximum

perceptible wavelength shift and demonstrated that the value plateaus around 30 nm. As concentration decreased below 500 pM, the magnitude of the redshift decreased following

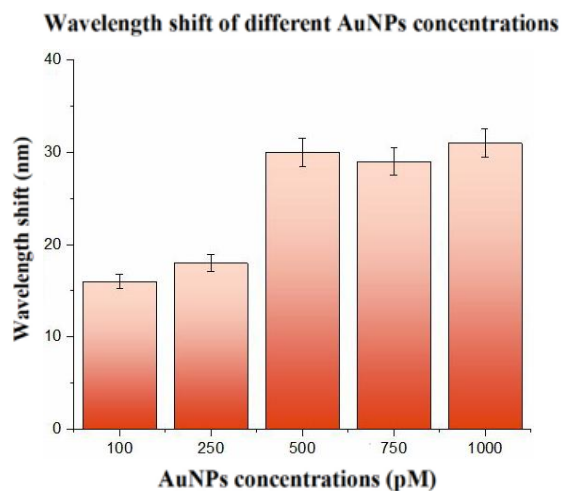


Figure 20: Observation of the effect concentration has on the LSPR resonant redshift.

an approximate S-curve. At a concentration of 250 pM and 100 pM, the wavelength delta was 18 nm and 15 nm, respectively. These low concentration values could occasionally produce the high ~30 nm shift, but it was inconsistent across multiple samples. As the concentration decreased, the difficulty in exactly locating the AuNP clusters surrounding a AuNM drastically increased since fewer aggregates would form altogether. The clusters that did form would contain fewer particles than at higher concentrations which diminishes the collective oscillation of AuNPs in large multimers, resulting in a weaker LSPR effect. For higher concentrations of AuNPs, a maximum redshift of 30 nm was the result of limiting available space surrounding the AuNMs. At higher concentrations more clusters would form around more AuNMs, but the size of the clusters would reach a maximum value. This means higher concentrations above 500 pM are easier to detect but do not produce a stronger wavelength delta as the value increases.

The formation of the clusters was verified by scanning electron microscope (SEM) imaging. In these images, the AuNP-AuNM coupling is easily observable as small 40 nm particles are visible in the post imaging (**Figure 21**, right) but only in close proximity to

that of the AuNM. These particles are missing in the images taken before the introduction of the AuNPs (**Figure 21**, left), further helping

to verify the formation of desirable aggregates.

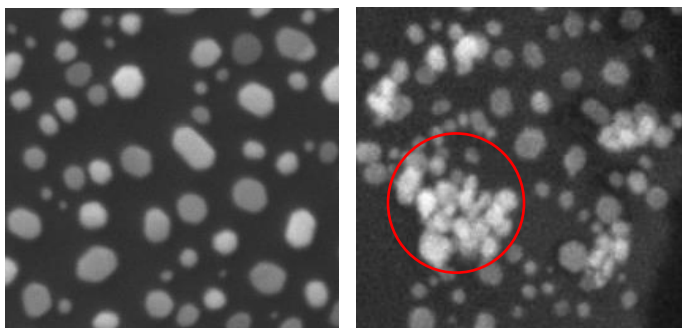


Figure 21: SEM images taken of the AuNM substrate before (left) and after (right) the addition of AuNPs.

6.0 Verification of Binding via Simulations and Modelling

The binding event studied by the above results was further confirmed by 3-D finite-difference time-domain (FDTD) simulations. Here, the system was modeled for a single AuNM, constructed as a hemispherical cap located on a pillar of equal diameter, with a maximum of six uncoated AuNPs surrounding the structure using a commercial software package (Lumerical Inc.). These particles were randomly oriented to mimic the actual binding of the AuNPs. To achieve this, the AuNPs and AuNM were set at fixed diameters of 40 nm and 100 nm, respectively. The AuNM diameter was approximated based on the average size gathered from the SEM images in **Figure 21**, while the AuNPs have far less deviation and were consistently 40 nm in diameter.

From the 3D modeling, a simulated absorption spectrum was produced for a AuNM surrounded by 0, 1, 2, 4, and 6 AuNPs. From this plot shown in **Figure 22** (middle), the bare AuNM showed a similar peak value to that of our actual substrate at approximately 580 nm. When 1 and 2 AuNPs were introduced a shift less than 10 nm was observed. This

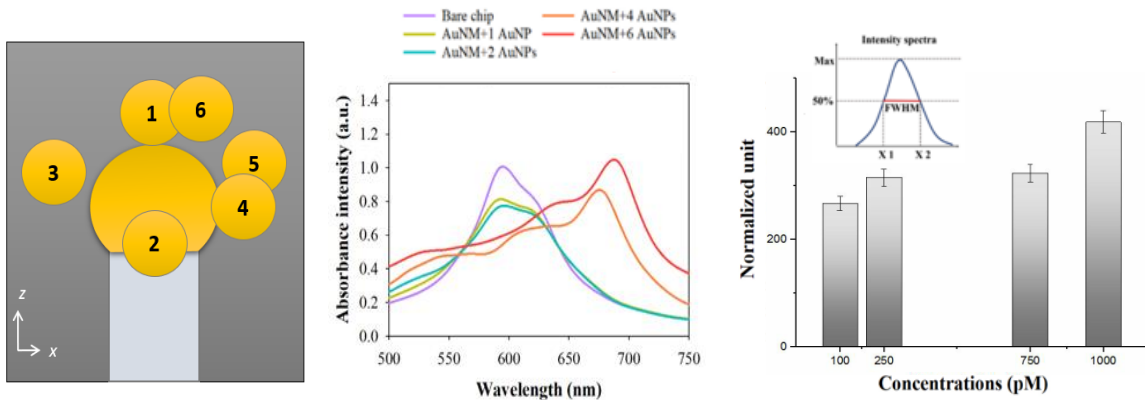


Figure 22: FDTD simulations were modeled according to the structures built (left). The resulting absorbance spectra for various numbers of AuNPs are shown (middle). This is compared to the experimental data put against a normalized unit (right) to demonstrate broadening.

coincides with the experimental values shown for lower concentrations of AuNPs. At these low concentrations, smaller clusters are likely to form and at farther distances from the 3AuNM, such that the resultant redshift will be smaller than that for higher concentrations. The simulation model accurately supports the experimental result seen for small clusters or dimers producing a miniscule shift with sparse simulated AuNPs exhibiting a similar minute shift. The simulations containing the 4 and 6 AuNPs produced a drastic redshift in peak wavelength, approaching 70 nm in magnitude. These conclusions are similar to that of the experimental results for large groupings and clusters, but to a greater extent. The difference in redshift is due to multiple factors, with the greatest factor being the AuNPs lacked the streptavidin coating. The coating on the experimental particles increased the spacing between the AuNP-AuNM coupling which is directly correlated to the strength of the hotspot and the magnitude of the resulting peak wavelength change [14]. Another difference that influenced the larger shift is the single AuNM pillar, which can ignore any effects due to surrounding nanostructures that could alter the localized RI. As well as the presence of remaining PBS molecules from the washing protocol which can have an effect on the RI and the incoming light. For the simulations with a greater number of AuNPs, the broadening effect becomes prominent as previously mentioned. This helps to further support the experimental data along with the SEM imaging, where the clusters were observed. Since particles can resonate in-phase or out-of-phase, these larger clusters undergo higher-order oscillations resulting in the broadening effect observed both experimentally and from the simulations [60]. Taking the experimental spectra from the concentration testing and applying a normalized unit, the increase in broadening is obvious at higher concentrations (**Figure 22**, right). The normalized unit was calculated by taking

the full width at half maximum (FWHM) value and dividing it by the peak intensity value. From this, as the concentrations increased, the normalized unit grew which indicates a broader spectrum at these greater concentrations. This follows the same trend observed by the simulated spectra for the increasing AuNP number.

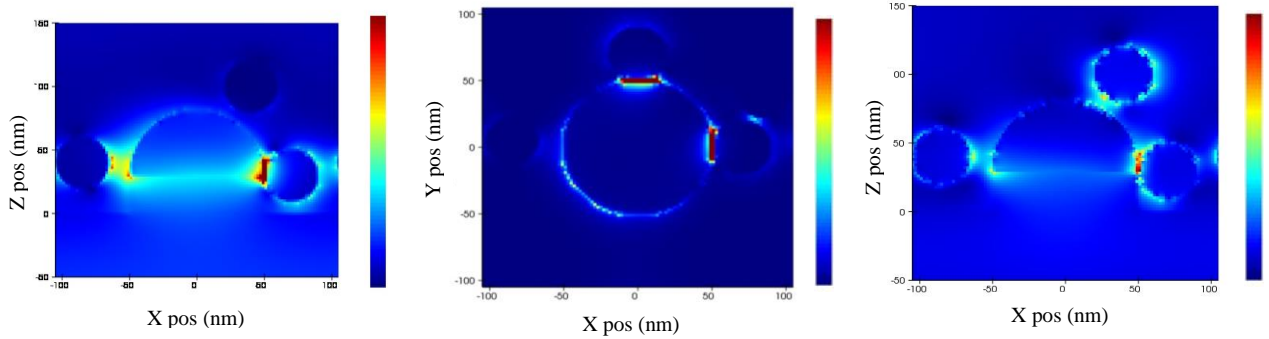


Figure 23: Electric field maps were produced for various *XY* (middle, right) and *XZ* (left) cross-sections of the AuNM with six AuNPs based on the simulations above. This was performed with the EM field polarized on the *x*-axis (left) and 45-degree angle (middle, right). These images were produced for 631 nm (left) and 623 nm (middle, right).

Electric field distribution maps were also modeled for the same AuNP-AuNM system as described above, but with only three surrounding particles. This method provides a technique used to observe the location of intense electric fields, or the “hot spots” previously described which in **Figure 23** are illustrated by the dark red spots. These images were formed based on linear polarization of the electric field from incoming photons, taken for cross-sections of the nanostructures at peak wavelength values of 623 and 631 nm. For this, the light underwent polarization on the *x*-axis or at a 45 degree angle. Focusing on the hotspots, an increased electric field intensity is observed between AuNPs bound in close proximity to the AuNM. As the distance between the two particles grows, the intensity decreases as shown by the change from the dark red color to a yellow hue. The shift in color coincided with a weaker “hot spot” where a lesser LSPR effect would be observed. As this was modeled using bare AuNPs, they were able to be located in closer proximity

than that of the actual experimental particles. Therefore, hotspots observed here were stronger and would produce a greater enhancement factor and redshift.

A final verification for the experimental conclusion was done through modeling the AuNP-AuNM coupling as a plasmonic ruler system. Noted below as equation 1, the formula was developed to calculate the wavelength delta that would result from particles

$$\frac{\Delta\lambda}{\lambda_0} = 0.12 \exp\left\{\frac{(-s/D)}{0.16}\right\} \quad (1)$$

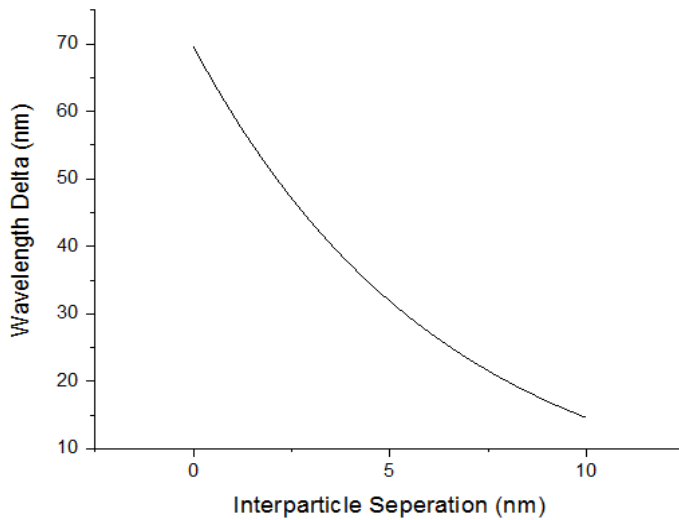


Figure 24: The calculated wavelength delta from interparticle separation based on the plasmonic ruler equation (Eqn #1).

with a known interparticle separation [61, 62]. This equation has been adapted for AuNP-AuNP coupling, as well as AuNP-Au film binding events [61,62]. Here, the AuNMs were treated as AuNPs for the relevant decay constant, as the advantage of the unique nanoscale geometries is a constrained AuNP that provides

more surface area than a gold film, but the stabilized advantage of a substrate [23]. For this application, the interparticle separation is unknown since the binding of the AuNP to the AuNM is a direct addition method that is a linker-free application. Therefore, the AuNP is randomly bound to the substrate with an affinity for the AuNM, not at an exact controlled distance. From this, the interparticle separation is calculated with a known delta wavelength of 30 nm. The particle diameter was set at 40 nm, and the initial wavelength of the system was 580 nm which is the average resonant peak for the AuNM substrate. This

initial value varied slightly between samples due to differing characteristics in the SiO₂ substrate. As mentioned previously, the decay constant was set for a AuNP dimer at 0.16 with a universal trend constant of 0.12 for AuNPs [62]. Based on the equation for a 30 nm wavelength shift, the according interparticle separation would be approximately 5 nm. This can be seen in **Figure 24** where the known wavelength delta accurately matches the interparticle separation for a streptavidin coating. An approximate 5 nm hydrodynamic diameter on the surface of a AuNP was due to the streptavidin molecule which was used for these experiments [63]. Therefore, the modeling for the plasmonic ruler with the AuNP and AuNM system corresponded accurately with the experimental results produced from the LSPR hot spots. This, in combination with the FDTD method and electric field distribution map modelling aids in supporting the conclusions drawn by the experimental results.

7.0 Demonstration of System for Detecting a Viral Target

7.1 Preparation of CRISPR Reagents

For proving an application of the microfluidic cell, Lbu-Cas13a proteins were employed to combine the advantageous effects of LSPR with CRISPR. This protein was prepared from a previous protocol as published and described [64]. For the CRISPR application, SARS-CoV-2 (703 nucleotides) spike genes were used as the positive target, while the SARS-CoV-1 (660 nucleotides) virus was used as the negative control alongside a sample with no target present. Both viruses were amplified from plasmids pUC57-SARS-CoV-1 and pUC57-SARS-CoV-2. This system used the same streptavidin-coated 40 nm AuNPs (nanoComposix Inc.) in combination with Dynabeads™ MyOne™ Streptavidin C1 (Thermal Fisher Scientific Inc.), also referred to as magnetic beads (MB) with a diameter of 1 μm . The RNA reporters and guide RNA used were acquired from IDT Inc. (Table S1) while the biotinylated anti-fluorescein antibodies (1 mg/mL) used were purchased from Vector Laboratories Inc.

7.2 Adaptations for the CRISPR Application

A final change was made to the direct addition protocol for the testing of an off-chip CRISPR-Cas13a procedure where the AuNPs were conjoined to a MB via FAM-ssRNA-biotin linkers. The CRISPR-LSPR combination is demonstrated by the schematic in **Figure 25** where a ssRNA reporter probe, labeled with a FAM and biotin component on opposing sides, was used for the formation of the AuNP-RNA-MB complex. In the presence of the target SARS-CoV-2 strand, the CRISPR-Cas13a complex binds to the

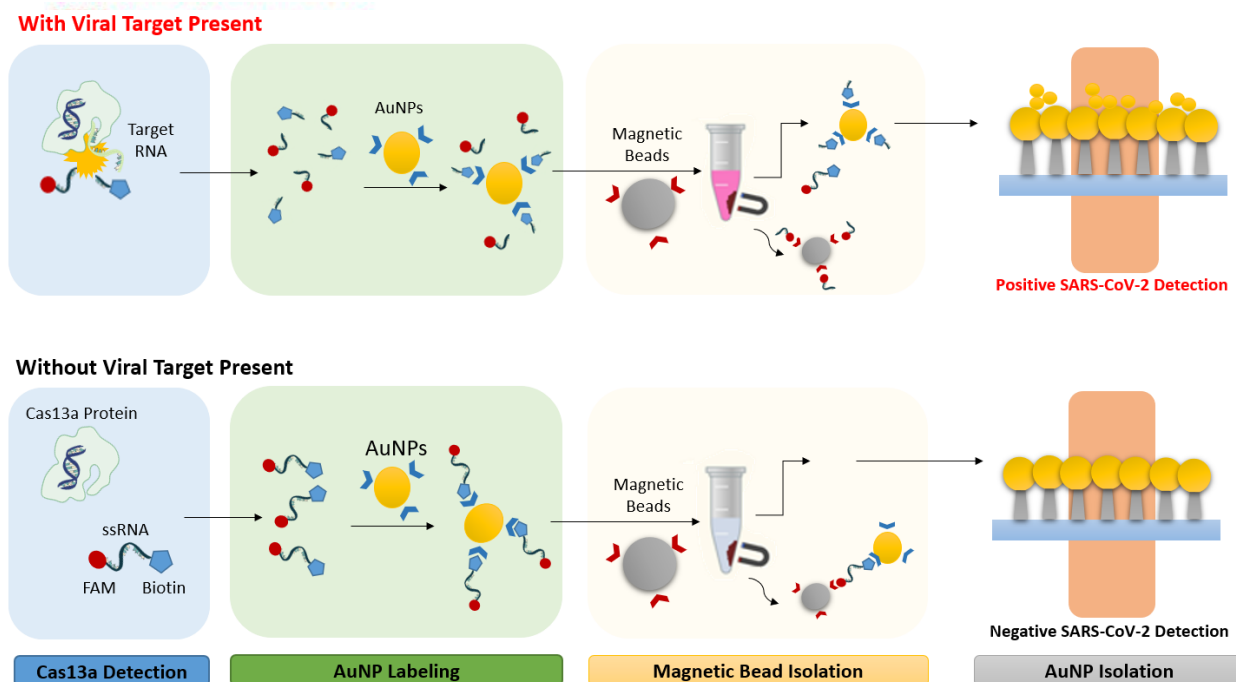


Figure 25: Diagram of the off-chip cleavage activity in the presence of a target and non-target sequence for the release and application of AuNPs to the AuNM substrate.

target RNA which promotes the collateral cleavage ability of the protein. This separated the FAM dye from the biotin by breaking the ssRNA reporters. The addition of AuNPs with a streptavidin coating favor binding to the biotin linker, which in the presence of the target, was previously separated from the FAM linker. Once the MBs are suspended, they preferentially bind to the FAM labels from the broken RNA probes. Without the SARS-CoV-2 target, the AuNP becomes linked to the MB with the probe conjoining them. Following this, the MB was isolated on the sidewall of the test vial using a magnet and the remaining supernatant solution was extracted. The supernatant solution was then diluted following the direct addition protocol for on-chip testing of the AuNM substrate seen in section 9.5. If the probe is cleaved by the presence of the target, the AuNPs are not isolated on the side wall since they are not adhered to the MB, and therefore left suspended in the supernatant. The presence of the AuNPs allow for positive identification of the target by detection of the resonant wavelength shift as described previously. If no wavelength shift

was observed, the AuNPs were not separated from the MB which indicates a lack of cleavage from the CRISPR-Cas13a protein and a lack of viral target in the sample.

7.3 Identification of the Viral Target

The experimental results gathered from the CRISPR testing demonstrated that the system was able to positively identify the SARS-CoV-2 target strand by a 23 nm redshift. The resulting shift was much larger than that of a similar non-target strand in SARS-CoV-1 and a negative control which showed a 12 nm and 10 nm redshift respectively, which can be seen in **Figure 26**. The ability to differentiate between the two RNA strands shows the specificity of the Cas13a protein to distinguish SNV, as well as produce a positive result far greater than the control sample. Both negative samples still exhibited a small redshift due to imperfect isolation of the MBs which still allowed for low concentrations of AuNPs to be added to the surface of the plasmonic chip. The magnitude of the SARS-CoV-2 redshift was lesser than that of the previous tests due to the portions of ssRNA that were attached to the biotin

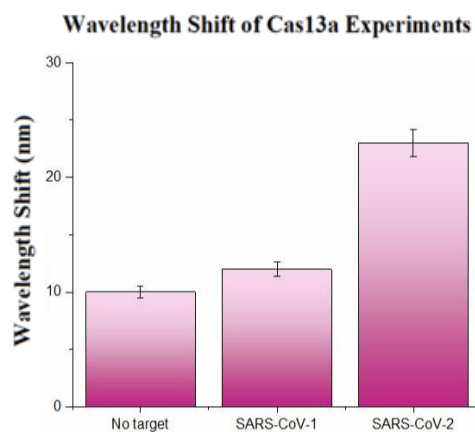


Figure 26: The resulting redshift from the CRISPR application for samples containing target RNA sequences.

label. The biotin would adhere to the streptavidin layer and further separate the AuNP from the AuNM, as demonstrated by the plasmonic ruler modeling. Other reasons could be the presence of the cleaved components, MBs, or the Cas13a protein in the supernatant that would alter the RI and diminish the strength of the LSPR effect between the AuNP and AuNM couple.

8.0 Conclusion & Future Work

Through this work, a highly sensitive microfluidic cell that was able to accurately detect ultra-dilute concentrations of AuNPs was developed. Incorporating a simplified direct addition protocol, it was possible to bind particles to unique nanoscale geometries constructed on a substrate, referred to as AuNMs. The system is able to positively identify the presence of AuNPs on the surface through LSPR detection, which takes advantage of changes in the local RI surrounding the substrate. The physical phenomenon investigated in this work provides a drastic enhancement to incident photons applied to the surface, which allow for the absorption spectrum of AuNPs with a concentration as low as 100 pM to be detected far above the background noise of spectrometers. The optimal conditions for AuNP addition, as gathered by this work, include concentrations greater than 500 pM for consistent results with a resonant shift greater than 30 nm. Other key parameters include the use of 40 nm AuNPs which exhibited the greatest redshift when compared to particles with a diameter of 4 nm, 100 nm, and 200 nm. As well as the streptavidin coating on AuNPs which was preferable to the bare AuNPs that were suspended in a sodium citrate solution. The bare particles would offer a greater redshift, but the charge neutralizing citrate molecule limited the aggregation and made them unusable particles for this application. The customizability of the LSPR binding allows for a variety of applications of the microfluidic cell. In this work, we combine the unique advantages of LSPR biosensing with a CRISPR-Cas13a complex for the detection of the SARS-CoV-2 RNA target. The combination of these two techniques forms a novel device that takes advantage of both of these unique methods for the first time. The use of the Cas13a protein provides the advantage of collateral cleavage to further increase the sensitivity of the system as well as

high specificity in discerning between SARS-CoV-2 and SARS-CoV-1 due to nucleotide variations.

To further understand the CRISPR application, the future work will investigate the effects of concentration on the cleavage capability of the Cas13a protein. Understanding the role of the ssRNA concentration will help determine the limit of detection for the off-chip cleavage before applying the supernatant to the AuNM substrate. Thereby uncovering the capabilities of the LSPR system for the dilute detection of viral targets. Focusing on the AuNP-AuNM cleavage, future experiments could be done to investigate the effect of particle shape on the resonant wavelength shift. Gold nanorods or nano-urchins might be able to increase the redshift due to the aspect ratio or spikes being able to achieve closer proximity or packing surrounding the AuNM.

9.0 Supplemental Information

9.1 Microfluidic Cell Fabrication

The device was constructed from PDMS adhered to a glass substrate. The PDMS was formed by mixing 50 g of silicon elastomer base with 5 g of curing agent (SILYARD 184) in a 10:1 ratio. This was poured over the resin mold in a petri dish. The mixture was added to a vacuum chamber for 30 minutes to remove all air bubbles that were introduced by the mixing. Following this, the petri dish containing the PDMS mixture was added to an oven at 75°C for 5 hours. This may take a longer heating time depending on the hardness of the PDMS before removing the resin mold with an X-acto knife. The PDMS was cut to the exact size of the resin mold, approximately 4 x 4 cm. This PDMS mold was immediately washed in acetone and a 50/50 ethanol and DI water mixture in two separate passes through an ultrasonic bath for 5 minutes. A glass slide underwent an identical washing procedure. Both samples were dried with a blast of air before being treated with an O₂ plasma for 15 seconds on the surfaces of the PDMS and glass that will be in contact with one another. The PDMS layer had two 1 mm holes punched into opposing corners of the molding to function as the inlet and outlet ports. Before adherence of the PDMS to the glass backing, a 2 x 2 cm portion of washable double-sided tape is cut and used to hold the AuNM chip in place within the cell. The PDMS is finally used to cover the AuNMs and adhered to the glass substrate while on a 125°C hot plate for 24 hours. The total volume remaining in the chamber was 240 µL which was used for the experimental solutions.

9.2 Absorbance Setup Construction

The system used to detect the absorbance spectrum for the AuNM substrate was constructed within our lab from a halogen light source, an ocean optics spectrometer, and

a set of filters. This included a UV-Vis collimating lens, a dielectric broadband mirror, and a short-pass filter. A collimating lens is used to orient the light beams into a parallel orientation, while the short-pass filter is responsible for blocking longer wavelengths and allowing shorter wavelengths to pass through, such as the visible spectrum, used in this application. The dielectric broadband mirror was used to reflect all light to ensure a greater percentage of light makes it to the surface of the AuNMs. The light source introduces photons to the surface of the AuNM system while the detector is underneath the stage, detecting the light that passes through the plasmonic chip.

9.3 Thiol and Salt Aging Protocol

1. Add 1 μM biotin-ssDNA-thiol modified probes (2.5 μL) to 1.1 nM of AuNP solution (10 μL) for 30 min mixing step
 - /5Biosg/ TT TCT GTC GCG CTT TTT /3ThioMC3-D/
 - 40 nm streptavidin coated AuNPs
2. Treat 1 μM thiol-oligonucleotides-AuNP with 100 μM TCEP (2.5 μL) for 2 hrs @ 25C
3. Apply reduced thiol-DNA with nuclease-free water (135 μL) to the AuNM for 12 hrs @ 25°C
4. Add 20 μL of 1 M NaCl five times at 1 hr intervals
 - Following each addition, sonification of the device for 10 s
5. Store @ 25°C for 24 hrs
6. Wash 3 times (730 μL / each time) with buffer (0.01 M phosphate buffer, pH 7.4)
 - Add .05% Tween20 for stabilizer (Was not added for following data)
7. Allow the samples to dry before recording absorbance measurements
 - Store at -20C while not in use to prevent degradation and altercations to the surface condition

9.4 Direct Addition Protocol

1. Add .5 μL of FAM DNA (100 μM) to 7 μL of 40 nm Strep GNP (1.1 nM) and set on shaker for 30 mins
 - If diluting, take .75 μL and dilute in DI water to desired concentration (i.e., 6.75 μL for 1:10 concentration)
 - If final dilution volume is greater than 7.5 μL , separate out 7.5 μL for next step
2. Treat 1 μM thiol-oligonucleotides-AuNP with 100 μM TCEP (2.5 μL) for 2 hrs @ 25°C
3. Add nuclease-free water (232 μL) to DNA-AuNP solution (7.5 μL) following by mixing with the vortex to ensure uniformity
 - Vary water volume as necessary: total volume should equate to ~240 μL

4. Apply mixture through inlet of plasmonic system for incubation overnight (~12 hrs @ RT) and wrap in parafilm to prevent evaporation or leakage
 - Add 30 min mixing step here as required for experiments
5. Wash 3 times (730 μL / each time) with 1x PBS buffer (0.01 M phosphate buffer, pH 7.4)
 - Washed using mechanical pump at a flow rate equal to 146 $\mu\text{L}/\text{min}$
 - First 250 μL collected in the first wash to observe color change before and after addition
6. Allow the samples to dry before recording absorbance measurements

9.5 Tables and Figures

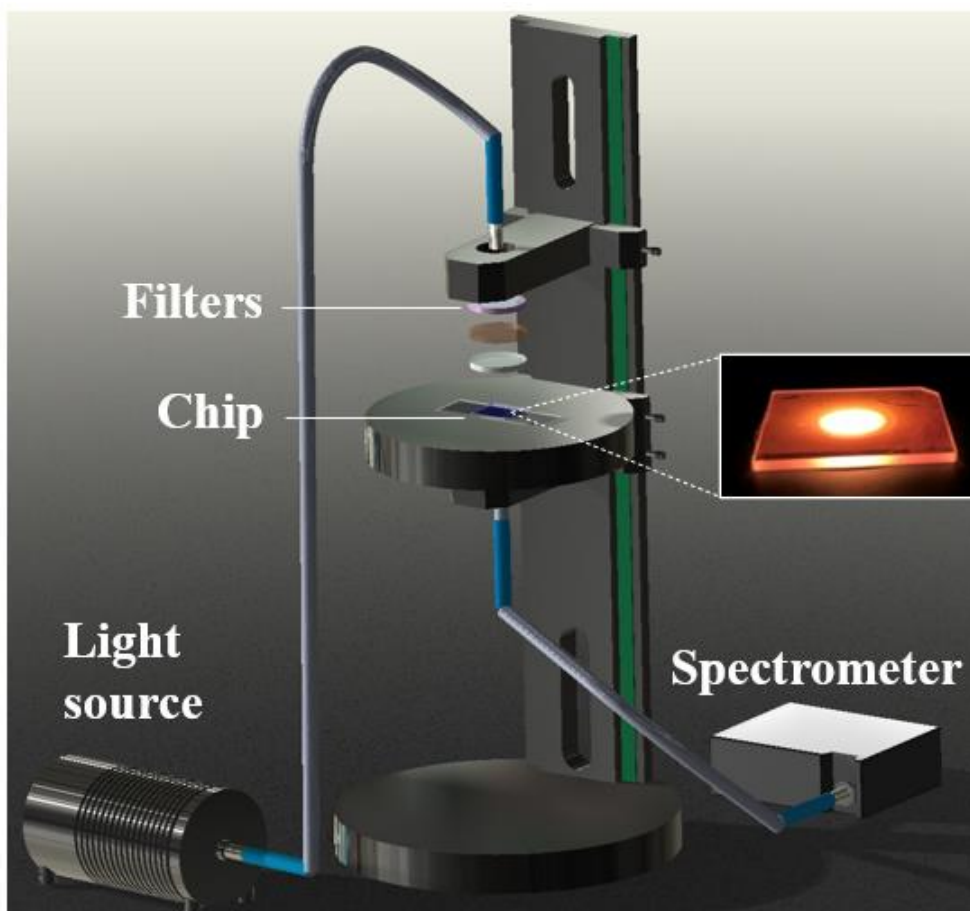


Figure S1. Schematic to illustrate the absorbance setup, including filter, light source, and stage. This used a light source on the surface of the chip with the detector underneath.

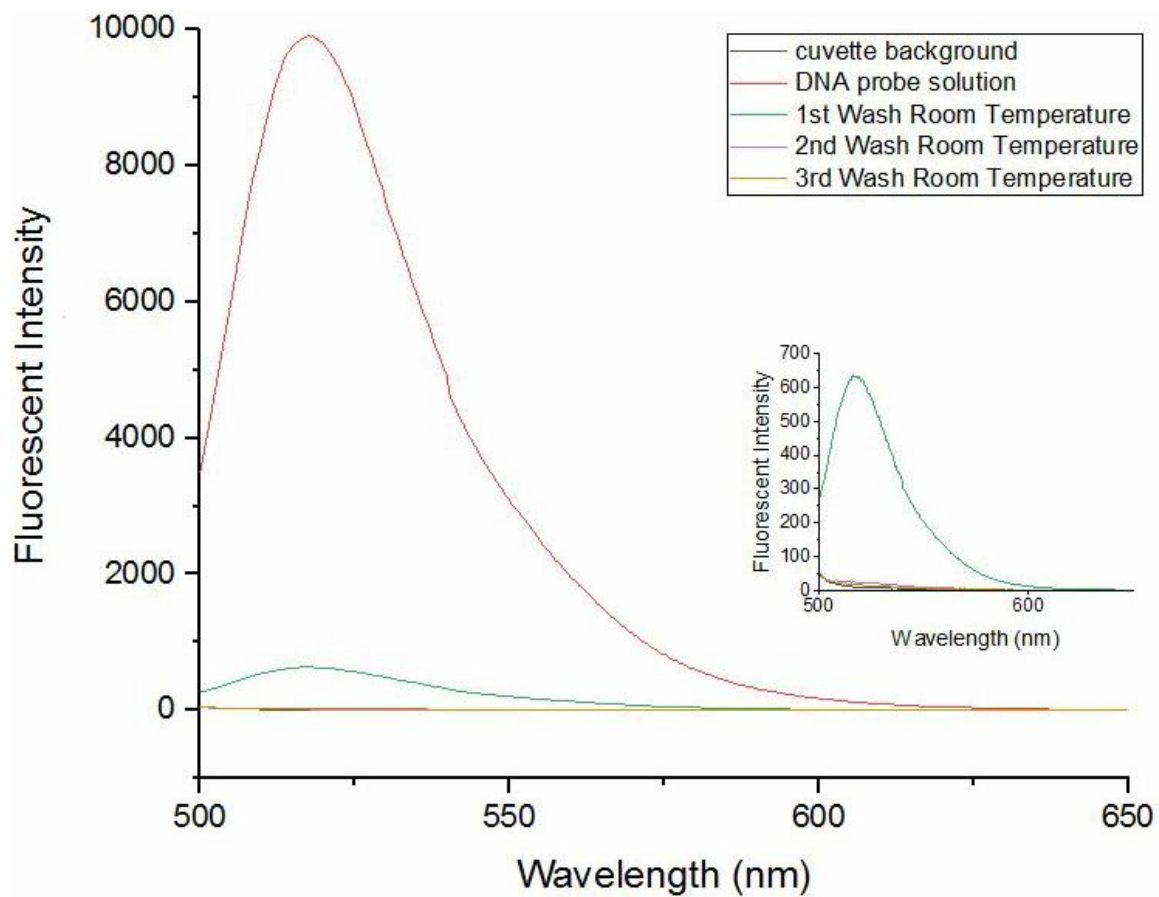


Figure S2. Graph to illustrate the fluorescent intensity of the DNA probe solution compared to washing solutions containing FAM-DNA probes and 1x PBS solution. Inset focuses on the three washing volumes for greater detail.

Table S1. Target RNA, crRNA, RNA reporter sequence.

Name	Sequence	Sources
Fragment of plasmids pUC57-SARS-CoV-2	UUAUGUCCUU CCCUCAGUCA GCACCUCAUG GUGUAGUCUU CUUGCAUGUG ACUUAUGUCC CUGCACAAGA AAAGAACUUC ACAACUGCUC CUGCCAUUUG UCAUGAUGGA AAAGCACACU UUCCUCGUGA AGGUGUCUUU GUUUCAAAUG GCACACACUG GUUUGUAACA CAAAGGAAUU UUUUAUGAACC ACAAUACA ACUACAGACA ACACAUUUGU GUCUGGUAAC UGUGAUGUUG UAAUAGGAAU UGUCAACAAC ACAGUUUAUG AUCCUUUGCA ACCUGAAUUA GACUCAUUCA AGGAGGAGUU AGAUAAAUAU UUUAAGAAUC AUACAUCACC AGAUGUUGAU UUAGGUGACA UCUCUGGCAU UAAUGCUUCA GUUGUAAAACA UUCAAAAAGA AAUUGACCGC CUCAAUGAGG UUGCCAAGAA UUUAAAUGAA UCUCUCAUCG AUCUCCAAGA ACUUGGAAAG UAUGAGCAGU AUAUAAAUG GCCAUGGUAC AUUUGGCUAG GUUUUAUAGC UGGCUUGAAU GCCAUGAUA UGGUGACAAU UAUGCUUUGC UGUAUGACCA GUUGCUGUAG UUGUCUCAAG GGCUGUUGUU CUUGUGGAUC CUGCUGCAA UUUGAUGAAG ACGACUCUGA GCCAGUGCUC AAAGGAGUCA AAUACAUA CACAUAACG AACUUAUGGA UUUGUUUAUG AGA	Synthego
Fragment of plasmids pUC57-SARS-CoV-1	UUGUGUUUAA UGGCACUUCU UGGUUUAUUA CACAGAGGAA CUUCUUUCU CCACAAUUA UUACUACAGA CAUACAUAUU GUCUCAGGAA AUUGUGAUGU CGUUAUUGGC AUCAUUAACA ACACAGUUUA UGAUCCUCUG CAACCUGAGC UUGACUCAUU CAAAGAAGAG CUGGACAAGU ACUUCAAAAA UCAUACAUCA CCAGAUGUUG AUCUUGGCGA CAUUCAGGC AUUAACGCUU CUGUCGUCAA CAUUCAAAAA GAAAUUGACC GCCUCAUGA GGUCGUAAA AAUUUAAAUG AAUCACUCAU UGACCUUCA GAAUUGGGAA AAUUGAGCA AUUAUUAAA UGGCCUUGGU AUGUUUGGCU CGGCUUCAU GCUGGACUAA UUGCCAUCGU CAUGGUUACA AUCUUGCUUU GUUGCAUGAC UAGUUGUUGC AGUUGCCUCA AGGUGCAUG CUCUUGUGGU UCUUGCUGCA AGUUUGAUGA GGAUGACUCU GAGCCAGUUC UCAAGGGUGU CAAAUACA UACACAUAAA CGAACUUAUG GAUUUGUUUA UGAGAUUUUU UACUCUUAGA UCAAUACUG CACAGCCAGU AAAAUUGAC AAUGCUUCUC CUGCAAGUAC UGUUCAUGCU ACAGCAACGA UACCGCUACA	Synthego
crRNA	GACCACCCCAAAAUGAAGGGGACUAAAACgccagagaugcaccuaau	IDT
RNA reporter	/56-FAM/rUrUrUrUrU/3BioTEG/	IDT

10.0 REFERENCES

- [1] Tang, Y.-W., Procop, G. W., & Persing, D. H. (1997). Molecular diagnostics of infectious diseases. *Molecular Diagnostics of Infectious Diseases*, 11, 18.
- [2] Paul, D., Kumar, A., Gajbhiye, A., Santra, M. K., & Srikanth, R. (2013). Mass Spectrometry-Based Proteomics in Molecular Diagnostics: Discovery of Cancer Biomarkers Using Tissue Culture. *BioMed Research International*, 2013, 1–16. <https://doi.org/10.1155/2013/783131>
- [3] Scigelova, M., Hornshaw, M., Giannakopoulos, A., & Makarov, A. (n.d.). *Fourier Transform Mass Spectrometry*. 19.
- [4] Heller, M. J. (2002). DNA Microarray Technology: Devices, Systems, and Applications. *Annual Review of Biomedical Engineering*, 4(1), 129–153. <https://doi.org/10.1146/annurev.bioeng.4.020702.153438>
- [5] Valones, M. A. A., Guimarães, R. L., Brandão, L. A. C., Souza, P. R. E. de, Carvalho, A. de A. T., & Crovela, S. (2009). Principles and applications of polymerase chain reaction in medical diagnostic fields: A review. *Brazilian Journal of Microbiology*, 40(1), 1–11. <https://doi.org/10.1590/S1517-83822009000100001>
- [6] Gubala, V., Harris, L. F., Ricco, A. J., Tan, M. X., & Williams, D. E. (2012). Point of Care Diagnostics: Status and Future. *Analytical Chemistry*, 84(2), 487–515. <https://doi.org/10.1021/ac2030199>
- [7] Huang, L., Ding, L., Zhou, J., Chen, S., Chen, F., Zhao, C., Xu, J., Hu, W., Ji, J., Xu, H., & Liu, G. L. (2021). One-step rapid quantification of SARS-CoV-2 virus particles via low-cost nanoplasmonic sensors in generic microplate reader and point-of-care device. *Biosensors and Bioelectronics*, 171, 112685. <https://doi.org/10.1016/j.bios.2020.112685>
- [8] Chin, L. K., Son, T., Hong, J.-S., Liu, A.-Q., Skog, J., Castro, C. M., Weissleder, R., Lee, H., & Im, H. (2020). Plasmonic Sensors for Extracellular Vesicle Analysis: From Scientific Development to Translational Research. *ACS Nano*, 14(11), 14528–14548. <https://doi.org/10.1021/acsnano.0c07581>
- [9] Petryayeva, E., & Krull, U. J. (2011). Localized surface plasmon resonance: Nanostructures, bioassays and biosensing—A review. *Analytica Chimica Acta*, 706(1), 8–24. <https://doi.org/10.1016/j.aca.2011.08.020>
- [10] Li, S., Miao, P., Zhang, Y., Wu, J., Zhang, B., Du, Y., Han, X., Sun, J., & Xu, P. (2021). Recent Advances in Plasmonic Nanostructures for Enhanced Photocatalysis and Electrocatalysis. *Advanced Materials*, 33(6), 2000086. <https://doi.org/10.1002/adma.202000086>
- [11] Chen, Y., & Ming, H. (2012). Review of surface plasmon resonance and localized surface plasmon resonance sensor. *Photonic Sensors*, 2(1), 37–49. <https://doi.org/10.1007/s13320-011-0051-2>

- [12] Chen, P., Chung, M. T., McHugh, W., Nidetz, R., Li, Y., Fu, J., Cornell, T. T., Shanley, T. P., & Kurabayashi, K. (2015). Multiplex Serum Cytokine Immunoassay Using Nanoplasmonic Biosensor Microarrays. *ACS Nano*, 9(4), 4173–4181. <https://doi.org/10.1021/acsnano.5b00396>
- [13] Gao, Y., Yuan, Z., & Gao, S. (2011). Semiclassical approach to plasmon–electron coupling and Landau damping of surface plasmons. *The Journal of Chemical Physics*, 134(13), 134702. <https://doi.org/10.1063/1.3575185>
- [14] Wang, C., Zhao, X.-P., Xu, Q.-Y., Nie, X.-G., Younis, M. R., Liu, W.-Y., & Xia, X.-H. (2018). Importance of Hot Spots in Gold Nanostructures on Direct Plasmon-Enhanced Electrochemistry. *ACS Applied Nano Materials*, 1(10), 5805–5811. <https://doi.org/10.1021/acsanm.8b01436>
- [15] Abudayyeh, O. O., Gootenberg, J. S., Konermann, S., Joung, J., Slaymaker, I. M., Cox, D. B. T., Shmakov, S., Makarova, K. S., Semenova, E., Minakhin, L., Severinov, K., Regev, A., Lander, E. S., Koonin, E. V., & Zhang, F. (2016). C2c2 is a single-component programmable RNA-guided RNA-targeting CRISPR effector. *Science*, 353(6299), aaf5573. <https://doi.org/10.1126/science.aaf5573>
- [16] Li, J., Sun, Y., Du, J., Zhao, Y., & Xia, L. (2017). Generation of Targeted Point Mutations in Rice by a Modified CRISPR/Cas9 System. *Molecular Plant*, 10(3), 526–529. <https://doi.org/10.1016/j.molp.2016.12.001>
- [17] Zhou, L., Peng, R., Zhang, R., & Li, J. (2018). The applications of CRISPR/Cas system in molecular detection. *Journal of Cellular and Molecular Medicine*, 22(12), 5807–5815. <https://doi.org/10.1111/jcmm.13925>
- [18] Vanegas, K. G., Jarczynska, Z. D., Strucko, T., & Mortensen, U. H. (2019). Cpf1 enables fast and efficient genome editing in *Aspergilli*. *Fungal Biology and Biotechnology*, 6(1), 6. <https://doi.org/10.1186/s40694-019-0069-6>
- [19] Han, W., & She, Q. (2017). CRISPR History: Discovery, Characterization, and Prosperity. In *Progress in Molecular Biology and Translational Science* (Vol. 152, pp. 1–21). Elsevier. <https://doi.org/10.1016/bs.pmbts.2017.10.001>
- [20] Nuñez, J. K., Kranzusch, P. J., Noeske, J., Wright, A. V., Davies, C. W., & Doudna, J. A. (2014). Cas1–Cas2 complex formation mediates spacer acquisition during CRISPR–Cas adaptive immunity. *Nature Structural & Molecular Biology*, 21(6), 528–534. <https://doi.org/10.1038/nsmb.2820>
- [21] Abi, A., & Safavi, A. (2019). Targeted Detection of Single-Nucleotide Variations: Progress and Promise. *ACS Sensors*, 4(4), 792–807. <https://doi.org/10.1021/acssensors.8b01604>
- [22] Mohanraju, P., Makarova, K. S., Zetsche, B., Zhang, F., Koonin, E. V., & van der Oost, J. (2016). Diverse evolutionary roots and mechanistic variations of the CRISPR-Cas systems. *Science*, 353(6299), aad5147. <https://doi.org/10.1126/science.aad5147>

- [23] Bhalla, N., Sathish, S., Galvin, C. J., Campbell, R. A., Sinha, A., & Shen, A. Q. (2018). Plasma-Assisted Large-Scale Nanoassembly of Metal–Insulator Bioplasmonic Mushrooms. *ACS Applied Materials & Interfaces*, 10(1), 219–226. <https://doi.org/10.1021/acsami.7b15396>
- [24] Mayeux, R. (2004). *Biomarkers: Potential uses and limitations*. 1(2), 7.
- [25] Strimbu, K., & Tavel, J. A. (2010). What are biomarkers?: *Current Opinion in HIV and AIDS*, 5(6), 463–466. <https://doi.org/10.1097/COH.0b013e32833ed177>
- [26] Gilboa, T., Garden, P. M., & Cohen, L. (2020). Single-molecule analysis of nucleic acid biomarkers – A review. *Analytica Chimica Acta*, 1115, 61–85. <https://doi.org/10.1016/j.aca.2020.03.001>
- [27] Xiao, M., Lai, W., Man, T., Chang, B., Li, L., Chandrasekaran, A. R., & Pei, H. (2019). Rationally Engineered Nucleic Acid Architectures for Biosensing Applications. *Chemical Reviews*, 119(22), 11631–11717. <https://doi.org/10.1021/acs.chemrev.9b00121>
- [28] Erlich, H., Gelfand, D., & Sninsky, J. (1991). Recent advances in the polymerase chain reaction. *Science*, 252(5013), 1643–1651. <https://doi.org/10.1126/science.2047872>
- [29] Gibson, U. E., Heid, C. A., & Williams, P. M. (1996). A novel method for real time quantitative RT-PCR. *Genome Research*, 6(10), 995–1001. <https://doi.org/10.1101/gr.6.10.995>
- [30] Freeman, W. M., Walker, S. J., & Vrana, K. E. (1999). Quantitative RT-PCR: Pitfalls and Potential. *BioTechniques*, 26(1), 112–125. <https://doi.org/10.2144/99261rv01>
- [31] Niemz, A., Ferguson, T. M., & Boyle, D. S. (2011). Point-of-care nucleic acid testing for infectious diseases. *Trends in Biotechnology*, 29(5), 240–250. <https://doi.org/10.1016/j.tibtech.2011.01.007>
- [32] Liu, P., Seo, T. S., Beyor, N., Shin, K.-J., Scherer, J. R., & Mathies, R. A. (2007). Integrated Portable Polymerase Chain Reaction-Capillary Electrophoresis Microsystem for Rapid Forensic Short Tandem Repeat Typing. *Analytical Chemistry*, 79(5), 1881–1889. <https://doi.org/10.1021/ac061961k>
- [33] Pumford, E. A., Lu, J., Spaczai, I., Prasetyo, M. E., Zheng, E. M., Zhang, H., & Kamei, D. T. (2020). Developments in integrating nucleic acid isothermal amplification and detection systems for point-of-care diagnostics. *Biosensors and Bioelectronics*, 170, 112674. <https://doi.org/10.1016/j.bios.2020.112674>
- [34] Holland, C. A., & Kiechle, F. L. (2005). Point-of-care molecular diagnostic systems—Past, present and future. *Current Opinion in Microbiology*, 8(5), 504–509. <https://doi.org/10.1016/j.mib.2005.08.001>
- [35] Rödiger, S., Liebsch, C., Schmidt, C., Lehmann, W., Resch-Genger, U., Schedler, U., & Schierack, P. (2014). Nucleic acid detection based on the use of microbeads: A

review. *Microchimica Acta*, 181(11–12), 1151–1168. <https://doi.org/10.1007/s00604-014-1243-4>

[36] Frank, L. A., & Krasitskaya, V. V. (2014). Application of Enzyme Bioluminescence for Medical Diagnostics. In G. Thouand & R. Marks (Eds.), *Bioluminescence: Fundamentals and Applications in Biotechnology—Volume 1* (Vol. 144, pp. 175–197). Springer Berlin Heidelberg. https://doi.org/10.1007/978-3-662-43385-0_6

[37] Yang, W., Tian, J., Ma, Y., Wang, L., Zhao, Y., & Zhao, S. (2015). A label-free fluorescent probe based on DNA-templated silver nanoclusters and exonuclease III-assisted recycling amplification detection of nucleic acid. *Analytica Chimica Acta*, 900, 90–96. <https://doi.org/10.1016/j.aca.2015.10.015>

[38] Wang, J. (2006). Electrochemical biosensors: Towards point-of-care cancer diagnostics. *Biosensors and Bioelectronics*, 21(10), 1887–1892. <https://doi.org/10.1016/j.bios.2005.10.027>

[39] Wang, J. (2002). Electrochemical nucleic acid biosensors. *Analytica Chimica Acta*, 9.

[40] Tan, A., Lim, C., Zou, S., Ma, Q., & Gao, Z. (2016). Electrochemical nucleic acid biosensors: From fabrication to application. *Analytical Methods*, 8(26), 5169–5189. <https://doi.org/10.1039/C6AY01221C>

[41] Wang, Y., Zhou, J., & Li, J. (2017). Construction of Plasmonic Nano-Biosensor-Based Devices for Point-of-Care Testing. *Small Methods*, 1(11), 1700197. <https://doi.org/10.1002/smtd.201700197>

[42] Tokel, O., Inci, F., & Demirci, U. (2014). Advances in Plasmonic Technologies for Point of Care Applications. *Chemical Reviews*, 114(11), 5728–5752. <https://doi.org/10.1021/cr4000623>

[43] Li, Z., Leustean, L., Inci, F., Zheng, M., Demirci, U., & Wang, S. (2019). Plasmonic-based platforms for diagnosis of infectious diseases at the point-of-care. *Biotechnology Advances*, 37(8), 107440. <https://doi.org/10.1016/j.biotechadv.2019.107440>

[44] Wang, D.-S., & Fan, S.-K. (2016). Microfluidic Surface Plasmon Resonance Sensors: From Principles to Point-of-Care Applications. *Sensors*, 16(8), 1175. <https://doi.org/10.3390/s16081175>

[45] Sepúlveda, B., Angelomé, P. C., Lechuga, L. M., & Liz-Marzán, L. M. (2009). LSPR-based nanobiosensors. *Nano Today*, 4(3), 244–251. <https://doi.org/10.1016/j.nantod.2009.04.001>

[46] Alaqad, K., & Saleh, T. A. (2016). Gold and Silver Nanoparticles: Synthesis Methods, Characterization Routes and Applications towards Drugs. *Journal of Environmental & Analytical Toxicology*, 6(4). <https://doi.org/10.4172/2161-0525.1000384>

- [47] Thakkar, K. N., Mhatre, S. S., & Parikh, R. Y. (2010). Biological synthesis of metallic nanoparticles. *Nanomedicine: Nanotechnology, Biology and Medicine*, 6(2), 257–262. <https://doi.org/10.1016/j.nano.2009.07.002>
- [48] Herrera, A. P., Resto, O., Briano, J. G., & Rinaldi, C. (2005). Synthesis and agglomeration of gold nanoparticles in reverse micelles. *Nanotechnology*, 16(7), S618–S625. <https://doi.org/10.1088/0957-4484/16/7/040>
- [49] Chan, W. C. W. (Ed.). (2007). *Bio-applications of nanoparticles*. Springer Science + Business Media ; Landes Bioscience.
- [50] Han, Y., Mayer, D., Offenhäusser, A., & Ingebrandt, S. (2006). Surface activation of thin silicon oxides by wet cleaning and silanization. *Thin Solid Films*, 510(1–2), 175–180. <https://doi.org/10.1016/j.tsf.2005.11.048>
- [51] Wang, M., Zhang, R., & Li, J. (2020). CRISPR/cas systems redefine nucleic acid detection: Principles and methods. *Biosensors and Bioelectronics*, 165, 112430. <https://doi.org/10.1016/j.bios.2020.112430>
- [52] Bao, M., Chen, Q., Xu, Z., Jensen, E. C., Liu, C., Waitkus, J. T., Yuan, X., He, Q., Qin, P., & Du, K. (2021). Challenges and opportunities for clustered regularly interspaced short palindromic repeats based molecular biosensing. *ACS Sensors*, 6(7), 2497–2522. <https://doi.org/10.1021/acssensors.1c00530>
- [53] van Dongen, J. E., Berendsen, J. T. W., Steenbergen, R. D. M., Wolthuis, R. M. F., Eijkel, J. C. T., & Segerink, L. I. (2020). Point-of-care CRISPR/Cas nucleic acid detection: Recent advances, challenges and opportunities. *Biosensors and Bioelectronics*, 166, 112445. <https://doi.org/10.1016/j.bios.2020.112445>
- [54] Pashchenko, O., Shelby, T., Banerjee, T., & Santra, S. (2018). A Comparison of Optical, Electrochemical, Magnetic, and Colorimetric Point-of-Care Biosensors for Infectious Disease Diagnosis. *ACS Infectious Diseases*, 4(8), 1162–1178. <https://doi.org/10.1021/acsinfecdis.8b00023>
- [55] Uppada, V., Gokara, M., & Rasineni, G. K. (2018). Diagnosis and therapy with CRISPR advanced CRISPR based tools for point of care diagnostics and early therapies. *Gene*, 656, 22–29. <https://doi.org/10.1016/j.gene.2018.02.066>
- [56] Hu, M., Yuan, C., Tian, T., Wang, X., Sun, J., Xiong, E., & Zhou, X. (2020). Single-Step, Salt-Aging-Free, and Thiol-Free Freezing Construction of AuNP-Based Bioprobes for Advancing CRISPR-Based Diagnostics. *Journal of the American Chemical Society*, 142(16), 7506–7513. <https://doi.org/10.1021/jacs.0c00217>
- [57] Hu, S., Huang, P.-J. J., Wang, J., & Liu, J. (2020). Dissecting the Effect of Salt for More Sensitive Label-Free Colorimetric Detection of DNA Using Gold Nanoparticles. *Analytical Chemistry*, 92(19), 13354–13360. <https://doi.org/10.1021/acs.analchem.0c02688>

- [58] Li, F., Zhang, H., Dever, B., Li, X.-F., & Le, X. C. (2013). Thermal Stability of DNA Functionalized Gold Nanoparticles. *Bioconjugate Chemistry*, 24(11), 1790–1797. <https://doi.org/10.1021/bc300687z>
- [59] Ojea-Jiménez, I., & Puentes, V. (2009). Instability of Cationic Gold Nanoparticle Bioconjugates: The Role of Citrate Ions. *Journal of the American Chemical Society*, 131(37), 13320–13327. <https://doi.org/10.1021/ja902894s>
- [60] Jackson, J. B., & Halas, N. J. (2004). Surface-enhanced Raman scattering on tunable plasmonic nanoparticle substrates. *Proceedings of the National Academy of Sciences*, 101(52), 17930–17935. <https://doi.org/10.1073/pnas.0408319102>
- [61] Jain, P. K., Huang, W., & El-Sayed, M. A. (2007). On the Universal Scaling Behavior of the Distance Decay of Plasmon Coupling in Metal Nanoparticle Pairs: A Plasmon Ruler Equation. *Nano Letters*, 7(7), 2080–2088. <https://doi.org/10.1021/nl071008a>
- [62] Bhalla, N., Formisano, N., Miodek, A., Jain, A., Di Lorenzo, M., Pula, G., & Estrela, P. (2015). Plasmonic ruler on field-effect devices for kinase drug discovery applications. *Biosensors & Bioelectronics*, 71, 121–128. <https://doi.org/10.1016/j.bios.2015.04.020>
- [63] D'Agata, R., Palladino, P., & Spoto, G. (2017). Streptavidin-coated gold nanoparticles: Critical role of oligonucleotides on stability and fractal aggregation. *Beilstein Journal of Nanotechnology*, 8, 1–11. <https://doi.org/10.3762/bjnano.8.1>
- [64] East-Seletsky, A., O'Connell, M. R., Knight, S. C., Burstein, D., Cate, J. H. D., Tjian, R., & Doudna, J. A. (2016). Two distinct RNase activities of CRISPR-C2c2 enable guide-RNA processing and RNA detection. *Nature*, 538(7624), 270–273. <https://doi.org/10.1038/nature19802>